Special Issue: SoTiC conference

International journal of spray and combustion dynamics

International Journal of Spray and Combustion Dynamics
1–24

DOI: 10.1177/17568277261463055
journals.sagepub.com/home/scd
Sage

Modelling thermoacoustic stability of cryogenic rocket engines with novel acoustic network model elements

Nicolas de Jong Cantarino[1,2], Wolfgang Armbruster[1], Justin Hardi[1], Michael Börner[1], Jan Martin[1] and Barry Zandbergen[2]

Abstract

Reliable and computationally efficient prediction capabilities for combustion instabilities in liquid propellant rocket combustion chambers are still rare. This study uses a low-order tool based on the well-known acoustic network model principle to map the stability limits of two different research rocket combustors with different cryogenic propellant combinations. New elements were derived capable of describing any isentropic background flow field in a contoured chamber, resolving acoustic chamber modes in three dimensions, and supporting distributed flame response models. Furthermore, an improved boundary condition element for the sonic throat of a rocket nozzle was implemented. The new network elements were benchmarked against two different research rocket combustion chambers, one single injector experiment using liquid oxygen and natural gas, exhibiting longitudinal mode instabilities and one multi-element thrust chamber with transverse mode instabilities. The acoustic resonant frequencies are predicted with an average absolute error of less than 5% for both cases. The tool is capable of predicting stability based on classical time lag and gain parameters applied to the new distributed flame model. The resulting stability maps are consistent with the benchmark cases for flame response time lags which are close to those reported in literature from computational fluid dynamics simulations and experiments.

Keywords

Thermoacoustics, acoustic network model, liquid propellant rocket engine, combustion instabilities, simulation

Received: 23 December 2025; accepted: 30 May 2026

Introduction

High-frequency (HF) combustion instabilities present a high risk for the development and testing of liquid-propellant rocket engines.[1,2] In the environment of extreme power density of rocket engine combustion chambers, pressure oscillations can potentially rapidly grow in amplitude leading to the destruction of the engine in a fraction of seconds.

Even though the phenomenon and the basic principle of thermoacoustics has been known for decades, predictive capabilities are still quite limited.[2–5] Consequently, instabilities are typically observed late in the engine development cycle during full-scale testing. In that case, a long and costly re-design and additional tests are required to solve the stability issue. A recent example is the Japanese LE-X demonstrator, a forerunner to the LE-9 cryogenic main engine, which also suffered from thermoacoustic instabilities.[6,7]

High-fidelity computational fluid dynamics simulations, like large eddy simulation (LES), have been reported to be able to predict combustion instabilities in sub-scale rocket combustion chambers. However, using LES to model the stability of full-scale flight engines is currently not feasible due to the very high computational costs. Nevertheless, great progress has been made in the modelling of sub-scale research combustors.[8–12] Some apply scale resolving approaches to reproduce instabilities.[13] Schmitt et al.[14,15] were able to simulate the natural transition to instability

[1]German Aerospace Center (DLR), Institute of Space Propulsion, Hardthausen, Germany
[2]Faculty of Aerospace Engineering, Delft University of Technology, Delft, the Netherlands

Corresponding author:
Wolfgang Armbruster, German Aerospace Center (DLR), Institute of Space Propulsion, Rocket Propulsion Technology Department, Im langen Grund, 74182 Lampoldshausen, Germany.
Email: Wolfgang.Armbruster@dlr.de

using this approach. An example of a less computationally expensive approach is the combination of Reynolds-averaged Navier-Stokes (RANS) and linearized Euler equation (LEE) simulation performed by Schulze.[11]

On the other hand, lower order models, like currently existing acoustic network models, have only limited success in predicting combustion instabilities in cryogenic rocket engines, even though they have been applied extensively to gas turbines. Specially due to the compact flame assumption, valid for gas turbines, being very far off from reality for rocket engines. Nevertheless, low-order approaches remain attractive for iterative design and quick parametric studies in the pre-development phases of new engines, or for time-critical analysis of engine test data.

In this article, a series of new low-order models will be presented. Said models are based on the same principles as the simpler wave equation approach and are therefore compatible with network model elements.

The analytical solution of the wave equation for constant background flow (derived in Poinsot[16]) shows that the acoustic variables can be related to a forward (f) and backward (g) propagating wave as shown in equation (1). In this work, it will be shown that for a more complex background flow (with axially-varying properties), the acoustic variables relate differently to the f and g waves.

$$\frac{\hat{p}}{\rho_0 c_0} = f + g \tag{1}$$

$$\hat{u} = f - g \tag{2}$$

The principle of network models, which the new developments are still compatible with, consists in representing a complex acoustic system through a series of simple elements. Based on geometry and flow properties, the system is divided into a series of elements for which the evolution of f and g is described analytically. At the interface between two elements f and g share the same value, which allows to describe the evolution throughout the entire system by building a system matrix containing the transfer matrices for f and g of the different simple elements. Special elements are designed for geometric discontinuities and for flow discontinuities (such as a compact flame). These elements also match the values of f and g at the interface with their adjacent elements, even though they are discontinuous themselves.

Once the system transfer matrix is set up, along with appropriate boundary conditions at the upstream and downstream boundaries (and at the radial and periodic boundaries for three-dimensional (3D) axisymmetric models), the acoustic resonant frequencies of the system can be obtained.

In summary, given the potential damage caused by combustion instabilities, their prediction early in engine development phases is critical. This study aims to improve the description of acoustics and flame response in rocket combustion chambers with newly derived models. These models were benchmarked against two different experimental cryogenic rocket combustors.

This article is structured as follows. First, a review of the state-of-the-art of low-order models is presented. Next, the derivation of the newly developed models is shown. Then, the experiments used for benchmarking are described. Finally, the comparison between simulation results and experimental data is presented.

State-of-the-art acoustic network models

Great introductions to acoustic network models are given by Poinsot[16] and Polifke et al.,[17] where the simple duct element with constant mean flow is presented. Application in gas turbines is common, such as the works by Huber[18] or Palies et al.[19] The application to rocket engines is more limited, with most work being focused on injector acoustic analysis.[11,20,21]

There have been multiple models developed with the aim to characterize the acoustics of systems with gradients in its background flow. Karthik et al.[22] obtain exact solutions with gradient background flow, but requires a constant temperature gradient and a very small Mach number. The model by Sujith et al.[23] allows for an arbitrary temperature gradient, but neglects the effects of mean flow ($M = 0$). Li and Morgans[24] developed a model for background flow gradients. It assumes all gradients are proportional to the density gradient, which for complex combustion processes such as a rocket engine is not applicable. It does not include area variations and it is only valid for longitudinal modes. Nicoud and Wieczorek[25] showed a model capable of describing gradients in background flow, which also considers the effects of the flame and entropy fluctuations. Nevertheless, the model is only capable of computing longitudinal modes. Schaefer and Polifke[26] developed a model that can describe arbitrary gradients, as well as cross-section area variations. The model offers great results for longitudinal mode prediction, but cannot model radial of tangential modes, which are of great importance for rocket engines. Cummings[27] also presents a model that allows for arbitrary background flow gradients. Although the model starts with the wave numbers of all three axis into consideration, in order to reach the desired analytical expression, it proceeds to consider only the plane mode (longitudinal), as well as assuming large frequencies of oscillation.

The simplest boundary conditions (BCs) are the ‘open’ and ‘closed’ ends, with reflection factors of -1 and 1, respectively. Many authors have worked on improving descriptions for BC, one example is the work by Davies[28,29] who offers a more complex BC for open ends, which depends on the frequency and the Mach number of the background flow. Experimental evidence shows that the reflection factor is bounded between the ideal open end and Davies model.

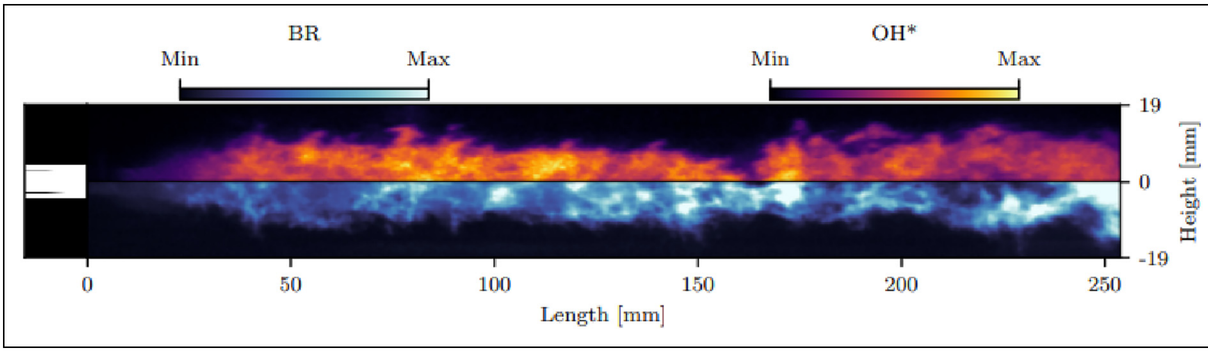

Figure 1. Image of a liquid oxygen-methane flame from experimental combustor Brenkammer N ('BKN').[47]

Regarding the description of the BC at the choked throat of a nozzle, of great interest for rocket engine applications, there are some relevant works to be mentioned. Firstly, the work of Marble and Candel[30] described a sonic BC at the throat, which is valid for low frequencies of osccilation. A later work by Duran and Moreau[31] expands on this work, extending the validity of the sonic BC to higher frequencies. This new model offers very good results when compared to experimental data, but requires a significantly more complex description than that of Marble and Candel.

There are various openly available tools for the modelling of thermoacoustic instabilities, all designed with gas turbine combustors in mind. One of said tools is 'OSCILLOS',[32,33] developed by the Imperial College of London. A different tool that uses the network model to simulate combustion instabilities is taX,[34] developed by the Thermo-Fluid Dynamics Group at TU München. Another open source solver, developed by Ekici et al.[35] is Helmholtz-X. A widely used open-source software is Nektar++ by the Imperial College of London.[36,37]

The tools presented are mainly meant for the simulation of combustion instabilities in gas turbines which typically have low Mach-number flow in the combustion chamber and only experience heat addition in a thin flame region. These conditions are remarkably different to a rocket engine in which flow speeds are higher and the flame is much longer (as shown in Figure 1). This further shows the need to develop a tool with a greater focus on rocket engines, in order to attempt to achieve consistent predictions of their stability in an early design phase.

In summary, great advances have been made in low-order acoustic modelling of complex flows. Nevertheless, the modelling of 3D modes (tangential and radial) is still an open problem. Furthermore, only the model by Schaefer et al. is capable of considering arbitrary gradients and area variations simultaneously. Lastly, none of the mentioned models can combine these effects with a distributed flame response throughout the entire chamber. Consequently, the need of new developments for rocket engine thermoacoustic simulation is clear.

Flame response modelling

The most common approaches to implement the flame response are flame transfer functions (FTFs), which are created from experimental data, and analytical models, which require an expression for the unsteady heat release. The most widely used unsteady heat release model is Crocco's simple time lag model.[38] There are other models, such as the ones by Polifke[39] with dual time delay models and distributed time delay models, as well as frequency dependent time delays. The report published by Casiano[40] summarizes multiple time lag models.

The time lag models need to be combined with a flame model. Examples valid for laminar premixed flames include the work by Polifke,[39,41] as well as from the OSCILLOS team.[32] These models are used to represent conical and wedge flames. Another work by Polifke et al.[42] slightly modifies the model based on the Rankine-Hugoniot equations and simple time lag model by introducing losses in the flame element. It introduces the pressure losses as a freely adjustable coefficient and names the model '$\tau - \zeta$ model', since it is based on Crocco's simple time lag also known as '$n - \tau$ model'.

Experimentally measured FTF can also be included in the network models, as shown by Schuermans et al.[43] This approach has become very common for gas turbine combustor modelling. A common approach to obtain the FTF is the multi-microphone method.[44]

In rocket engines, the measurement of time lags and gains is much more difficult than in gas turbine combustors. The work by Martin et al.[45] managed to obtain the time lag values for a sub-scale combustor, thanks to its large optical access. Obtaining an accurate experimental FTF for a rocket engine is yet to be achieved.

Limitations of existing network model elements for rocket combustion chambers

In the combustion chamber of a rocket engine, the gradients in the mean flow variables are significant. This is especially so for the speed of sound and density, which are key variables for acoustic analysis. Furthermore, these gradients extend throughout a significant length of the chamber, not allowing to consider them as discontinuities, contrary to the usual approach for gas turbine combustors. Moreover, the rocket engine nozzle also presents these strong gradients in mean flow along with a significant variation in area. Most importantly, tangential and radial modes are of high relevance for rocket engines, as they have been the cause of instability in the past.[46] As stated before, this generated a need to develop a set of new acoustic elements.

In gas turbine combustors, the compact flame assumption allows to model the entire flow as isentropic, with an entropy discontinuity at the flame. For rocket engines, due to slower atomization, evaporation and mixing, the flame length is of the order of the combustion chamber length (see Figure 1). This invalidates the compact flame assumption. Consequently, the entire flow-field needs to be solved as non-isentropic. This motivated the development of a distributed flame element which allows the spatial extent of the flame to be captured, as well as the previously described gradients in mean flow.

Novel models

In this section, the novel elements developed will be presented, showing their mathematical description and highlighting some key aspects. The full derivation for all the presented models is present in the Appendix.

One-dimensional (1D)-chamber with varying background mean flow and area

In this model, all the background flow variables are considered to be a known function of the axial coordinate. Both the background and acoustic flows are isentropic. The model allows for the computation of the longitudinal resonant frequencies of the system. The acoustic pressure and velocity are described as follows:

$$\hat{p} = \rho_0 c_0 \left(f e^{-ik_{f,p}(x)} + g e^{-ik_{g,p}(x)} \right) e^{i\omega t} \tag{3}$$

$$\hat{u} = \left(f e^{-ik_{f,u}(x)} - g e^{-ik_{g,u}(x)} \right) e^{i\omega t} \tag{4}$$

where the wave numbers $k_{f,p}$, $k_{g,p}$, $k_{f,u}$, and $k_{g,u}$ are a function of the axial coordinate and need to be computed. They can be obtained by solving a set of four uncoupled first-order ordinary differential equation (ODE):

$$i\left(1-M_0^2\right)\frac{\partial k_{f,p}}{\partial x} = \left(M_0^2 + 2M_0\eta_f - 1\right)\frac{1}{u_0}\frac{\partial u_0}{\partial x} + \left(1-M_0^2\right)\frac{1}{c_0}\frac{\partial c_0}{\partial x} - \frac{1}{A}\frac{\partial A}{\partial x} + \left(\eta_f - M_0\right)\frac{i\omega}{c_0} \tag{5}$$

$$i\frac{\partial k_{f,u}}{\partial x} = \left(\frac{M_0}{\eta_f} - \frac{2}{1-M_0^2} + 1\right)\frac{1}{u_0}\frac{\partial u_0}{\partial x} + \frac{1}{\eta_f}\frac{M_0}{1-M_0^2}\frac{1}{A}\frac{\partial A}{\partial x} + \frac{1}{M_0}\left(1 - \frac{1}{\eta_f}\frac{\eta_f - M_0}{1-M_0^2}\right)\frac{i\omega}{c_0} \tag{6}$$

The equations for $k_{g,p}$ and $k_{g,u}$ are identical to the ones for $k_{f,p}$ and $k_{f,u}$ respectively, but substituting η_f for η_g. The solution for the f and g waves differs due to the different upstream boundary conditions:

$$\eta_f(0) = 1, \quad \eta_g(0) = -1 \tag{7}$$

The function η is computed as $\eta(x) = e^{-i(k_u(x) - k_p(x))}$. The values of k for the acoustic pressure and velocity need to be different, or the expressions would not be a solution to the acoustic equations. If the gradients of background flow are removed, then they become equal and the solution corresponds to the uniform flow duct from literature (see explanation after equations (42) and (43)). For more details and the full derivation consult the Appendix ('Full derivation of 1D isentropic acoustics with area variation').

Sonic boundary condition

The expression for a sonic BC at the throat of a rocket engine (convergent to divergent transition) is:

$$i\omega\frac{\hat{p}}{\rho_0 c_0} - \left(i\omega + 2\frac{\partial u_0}{\partial x}\right)\hat{u} = 0 \tag{8}$$

Its derivation is present in the Appendix (equation (88)). The BC is meant to be used in this shape for the 1D isentropic element. Nevertheless, for a qualitative feel of what the BC represents, the acoustic pressure and velocity will be substituted by f and g (without correction factors), resulting in:

$$R_{Sonic} = \frac{g}{f} = \frac{\dfrac{\partial u_0}{\partial x}}{i\omega + \dfrac{\partial u_0}{\partial x}} \tag{9}$$

Note that for low frequencies, this approximate reflection factor equals 1 (closed BC) and for very high frequencies it approximates 0 (non-reflecting BC), which matches experimental measurements.[31,48] Keep in mind that this reflection factor is only qualitative, as it has been shown that for this model the expression for the acoustic velocity carries a correction factor for the f and g waves. For more details, consult the complete derivations in the Appendix (see equation (40)).

The sonic BC for an acoustic 3D non-isentropic flow is shown next. To obtain the 3D isentropic BC it is sufficient to substitute $\hat{\rho} = \frac{\hat{p}}{c_0^2}$ in the non-isentropic expression.

$$\left(i\omega - (1-\gamma)\frac{\partial u_0}{\partial x} + \frac{\partial c_0}{\partial x}\right)\frac{\hat{p}}{\rho_0 c_0} - \left(\frac{\partial u_0}{\partial x}\right)\frac{\hat{\rho}}{\rho_0/c_0} + \left(-i\omega - \frac{\gamma+1}{\gamma}\frac{\partial u_0}{\partial x} + \frac{2}{\gamma}\frac{\partial c_0}{\partial x}\right)\hat{u} + c_0\frac{\pi^2\beta_{m,n}^2}{R^2}\chi = 0 \tag{10}$$

3D element with varying background mean flow to model transverse acoustic modes

This model considers a known, purely axial background flow and a 3D acoustic flow. Both are considered isentropic. Cross-section area needs to remain constant. The model allows for the computation of the longitudinal, radial and tangential resonant frequencies of the system. The acoustic variables are described as follows:

$$\frac{\hat{p}}{\rho_0 c_0}(z,r,\theta,t) = J_n\left(\pi\beta_{m,n}\frac{r}{R}\right) \cdot \left(fe^{-ik_{f,p}(z)} + ge^{-ik_{g,p}(z)}\right)\left(Pe^{-in\theta} + Qe^{in\theta}\right)e^{i\omega t} \tag{11}$$

$$\hat{u}_r(z,r,\theta,t) = \frac{\partial J_n\left(\pi\beta_{m,n}\frac{r}{R}\right)}{\partial r} \cdot \left(\eta_{r,f}fe^{-ik_{f,p}(z)} + \eta_{r,g}ge^{-ik_{g,p}(z)}\right)\left(Pe^{-in\theta} + Qe^{in\theta}\right)e^{i\omega t} \tag{12}$$

$$\hat{u}_\theta(z,r,\theta,t) = J_n\left(\pi\beta_{m,n}\frac{r}{R}\right) \cdot \left(\eta_{\theta,f}fe^{-ik_{f,p}(z)} + \eta_{\theta,g}ge^{-ik_{g,p}(z)}\right)\left(Pe^{-in\theta} - Qe^{in\theta}\right)e^{i\omega t} \tag{13}$$

$$\hat{u}_z(z,r,\theta,t) = J_n\left(\pi\beta_{m,n}\frac{r}{R}\right) \cdot \left(fe^{-ik_{f,u}(z)} - ge^{-ik_{g,u}(z)}\right)\left(Pe^{-in\theta} + Qe^{in\theta}\right)e^{i\omega t} \tag{14}$$

where the exponents $k_{f,p}, k_{g,p}, k_{f,u}$, and $k_{g,u}$ need to be solved for along with the correction factors $\eta_{f,\theta}, \eta_{g,\theta}, \eta_{f,r}$, and $\eta_{g,r}$. Said correction factors can be related to χ_f, and χ_g, leading to a system of six uncoupled first-order ODE:

$$\begin{aligned} i\left(1-M_{z,0}^2\right)\frac{\partial k_{f,p}}{\partial z} = &-\frac{\pi^2\beta_{m,n}^2}{R^2}\chi_f M_{z,0} \\ &+ \left(M_{z,0}^2 + 2M_{z,0}\eta_{z,f} - 1\right)\frac{1}{u_{z,0}}\frac{\partial u_{z,0}}{\partial z} \\ &+ \left(M_{z,0}^2 + 1\right)\frac{1}{c_0}\frac{\partial c_0}{\partial z} \\ &+ \left(M_{z,0}(\eta_{z,f} + M_{z,0}) - 1\right)\frac{1}{A}\frac{\partial A}{\partial z} + (\eta_{z,f} - M_{z,0})\frac{i\omega}{c_0} \end{aligned} \tag{15}$$

$$\begin{aligned} i\frac{\partial k_{f,u}}{\partial z} = &\frac{i\omega}{M_{z,0}c_0} + \frac{1}{u_{z,0}}\frac{\partial u_{z,0}}{\partial z} \\ &+ \frac{1/\eta_{z,f}}{M_{z,0}}\left[\left(M_{z,0}^2 - 1\right)\frac{1}{u_{z,0}}\frac{\partial u_{z,0}}{\partial z} + \frac{1}{c_0}\frac{\partial c_0}{\partial z} - \frac{1}{A}\frac{\partial A}{\partial z} - i\frac{\partial k_{f,p}}{\partial z}\right] \end{aligned} \tag{16}$$

$$M_{z,0}\frac{\partial \chi_f}{\partial z} = 1 - \chi_f\left(\frac{i\omega}{c_0} - iM_{z,0}\frac{\partial k_{f,p}}{\partial z}\right) \tag{17}$$

The equations for f and g are once again identical to each other, with the difference residing in the upstream boundary conditions. Said boundary conditions can be found in the Appendix (see equation (79)), along with a careful derivation of the equations.

Distributed flame response model

The background flow is assumed to be purely axial but not isentropic, as there is a heat release along the length of the element function of the axial coordinate. The model allows to compute the resonant frequencies of the system, along with its stability. The acoustic pressure and velocity are described as shown for the 1D isentropic element in equations (3) and (4). For the distributed flame model, the acoustic density needs an additional description as follows:

$$\begin{aligned} \hat{\rho} &= \frac{\rho_0}{c_0}\left(\eta_{\rho,f}fe^{-ik_{f,p}(x)} + \eta_{\rho,g}ge^{-ik_{g,p}(x)}\right)e^{i\omega t} \\ \eta_{\rho,f} &= e^{-i(k_{f,\rho} - k_{f,p})}, \quad \eta_{\rho,g} = e^{-i(k_{g,\rho} - k_{g,p})} \end{aligned} \tag{18}$$

The wave numbers for pressure, velocity, and density need to be solved for, leading to a system of six uncoupled first-order ODE:

$$\begin{aligned} -i\frac{\partial k_\rho}{\partial x}\eta_\rho = &\left[-\frac{i\omega}{c_0}\frac{1}{M_0} + \frac{1}{c_0}\frac{\partial c_0}{\partial x}\right]\eta_\rho \\ &+ \frac{1}{M_0}\left[i\frac{\partial k_u}{\partial x} + \frac{1}{u_0}\frac{\partial u_0}{\partial x}\right]\eta_u \end{aligned} \tag{19}$$

$$\begin{aligned} i\frac{\partial k_u}{\partial x} = &\left[\frac{M_0}{u_0}\frac{\partial u_0}{\partial x}\right]\frac{\eta_\rho}{\eta_u} + \left[\frac{i\omega}{c_0}\frac{1}{M_0} + \frac{1}{u_0}\frac{\partial u_0}{\partial x}\right] \\ &+ \left[-\frac{i}{M_0}\frac{\partial k_p}{\partial x} + \frac{1}{M_0\rho_0}\frac{\partial \rho_0}{\partial x} + \frac{1}{M_0 c_0}\frac{\partial c_0}{\partial x}\right]\frac{1}{\eta_u} \end{aligned} \tag{20}$$

$$\begin{aligned} -i\left(1-M_0^2\right)\frac{\partial k_p}{\partial x} = &\left[-\frac{i\omega}{c_0} - \frac{1-\gamma}{\gamma}\frac{M_0}{A}\frac{\partial A}{\partial x}\right]\eta_u \\ &- \left[\frac{\gamma+1}{\gamma}\frac{M_0}{u_0}\frac{\partial u_0}{\partial x} + \frac{2}{\gamma}\frac{M_0}{c_0}\frac{\partial c_0}{\partial x}\right]\eta_u - \left[\frac{M_0^2}{u_0}\frac{\partial u_0}{\partial x}\right]\eta_\rho + \\ &+ \frac{i\omega}{c_0}M_0 + \left((1-\gamma)M_0^2 - 1\right)\frac{1}{\rho_0}\frac{\partial \rho_0}{\partial x} + \\ &+ \left(M_0^2 - 1\right)\frac{1}{c_0}\frac{\partial c_0}{\partial x} - M_0(\gamma-1)n_{flame}\frac{\gamma Q_0}{\rho_0 c_0^3}e^{-i\omega\tau} \end{aligned} \tag{21}$$

Table 1. Input parameters for the verification of the three-dimensional (3D) isentropic acoustic element.

L	R	P_{inj}	T_{inj}	$\dot{m}$	Fluid
0.05 m	40 mm	10 bar	150 K	10 kg/s	Nitrogen

Once more, the equations for the f and g waves are identical, differentiated through the upstream boundary conditions. For details, as well as the expressions of the 3D element, please refer to the Appendix (see 'Full derivation of 1D distributed flame model with area variation' in the Appendix).

For the results that will be subsequently presented, the unsteady heat release was modelled as follows:

$$\hat{\dot{Q}}(t,x) = \dot{Q}(x) n_{flame}(\omega, x) e^{-i\tau(\omega,x)\omega} \frac{\hat{p}(t,x)}{p_0(x)} \tag{22}$$

Furthermore, in this work, due to the limited experimental data available, both n and τ will be considered constant. Nevertheless, as is shown in detail in the Appendix, introducing any other description for the heat release is possible with this model as long as it is a linear function of the acoustic variables.

Verification of models

Multiple verification steps were taken for the first model. First, the expressions for the acoustic variables are a solution of the acoustic equations, as they have been derived fully analytically. Furthermore, if the gradients of area and background flow are removed from the isentropic elements, the solutions for the 1D and 3D incompressible ducts are retrieved, respectively, (see the Appendix, equations (42) and (43)). This shows that the new model correctly describes incompressible flows.

Further verification was performed using cases with moderate gradients in background flow and/or area. The new models require only one element to describe this behaviour. They were compared with network models made of multiple basic elements from literature. One of these verification cases is highlighted next.

The results of the novel 3D element are compared to the results of the literature 3D incompressible tube, those of simulating the system discretized into 100 3D uniform flow elements (approximation 1) and those of the same discretization but with added compact discontinuity elements between the 3D uniform flow tubes (approximation 2). Input parameters are summarized in Table 1. The results are shown in Table 2. Given its simplicity, it was to be expected that the single 3D uniform flow element would differ the most from the novel element. Furthermore, approximations 1 and 2 both match very closely the real part of the solution from the novel element, but only approximation 2 shows a similar behaviour of the imaginary component (to be expected given that approximation 1 only contains elements that conserve acoustic energy). This shows that the new model adequately describes resonant frequency and damping rate for moderate gradients. Note that, for the more extreme gradients present in a rocket engine and especially regarding the flame, the approximations made from the basic elements get worse, which is why the new elements are needed. Their performance in more complex systems will be shown in the Results section.

Table 2. Resonant frequencies of three-dimensional (3D) straight tube with major compressibility effects.

Mode	Novel element	3D uniform flow
T1	2379.22 + 48.23j	2513.62–1.63e−04j
T1L1	3983.05 + 49.26j	4234.04–1.33e−04j
T1L2	5735.99 + 49.67j	6105.33–6.50e−05j
T1L3	7533.85 + 49.43j	8022.61 + 1.08e−03j
T1L4	9350.69 + 49.55j	9959.34 + 4.12e−04j
Mode	**Appr. 1 solutions**	**Appr. 2 solutions .**
T1	2380.23 + 1.39e−04j	2383.01 + 37.21j
T1L1	3987.29 + 4.58e−05j	3986.14 + 48.80j
T1L2	5740.57 + 1.29e−04j	5737.22 + 52.39j
T1L3	7538.70 + 1.00e−03j	7533.53 + 53.99j
T1L4	9355.87 + 4.36e−05j	9349.01 + 54.95j

A more extreme example was also tested, where two tubes connected through an area discontinuity are considered. Both have a length of 0.05 m, left tube with area 10^{-5}m^2 and right tube 10^{-4}m^2. The upstream conditions are 10 bar, 200 K and 0.001 kg/s, with nitrogen as the working fluid. No losses are considered. A comparison is made between the new 1D isentropic element (capable of modelling the entire system on its own) and a combination of two uniform flow ducts and the area discontinuity element from literature. In Figure 2, the results for the new model are shown and in Figure 3, the results of the literature model are superimposed on top of the new models. Both match very close both in resonant frequency and mode shape. This shows that the new model also converges to the compact limit. Note that the new model is not meant to be used in such a simple case where literature elements fit better, but it does show that the new element is capable of modelling very large gradients in background flow.

Consequently, the new models have been shown to converge to the incompressible and compact solutions (no gradients and 'infinite' gradient, respectively), as well as always being solutions to the acoustic equations. This justifies going further into validation against experimental data.

Computational framework

The software LORESA was developed at DLR, in which these new models were implemented. Said software was

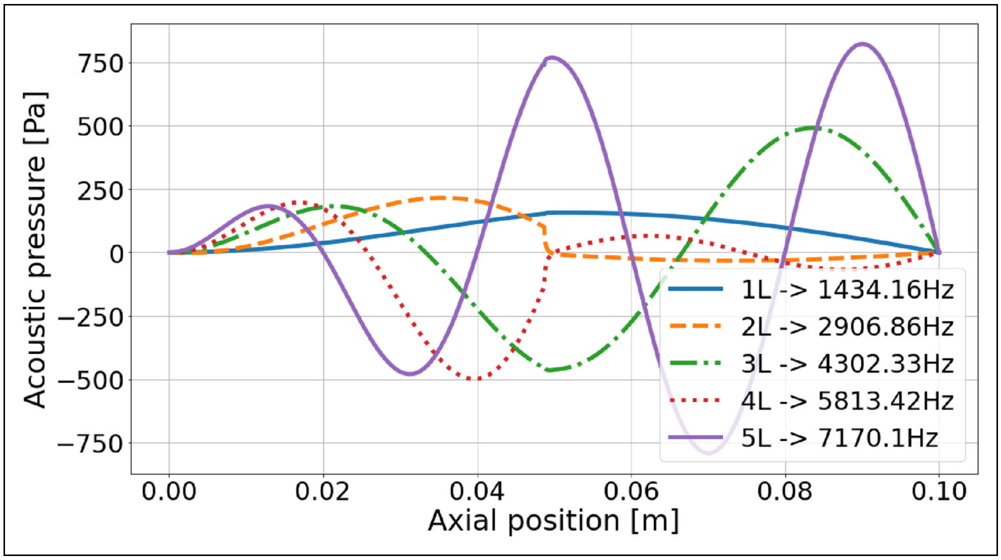

Figure 2. Modelling of a compact discontinuity between two straight tubes with the newly introduced one-dimensional (1D) isentropic element.

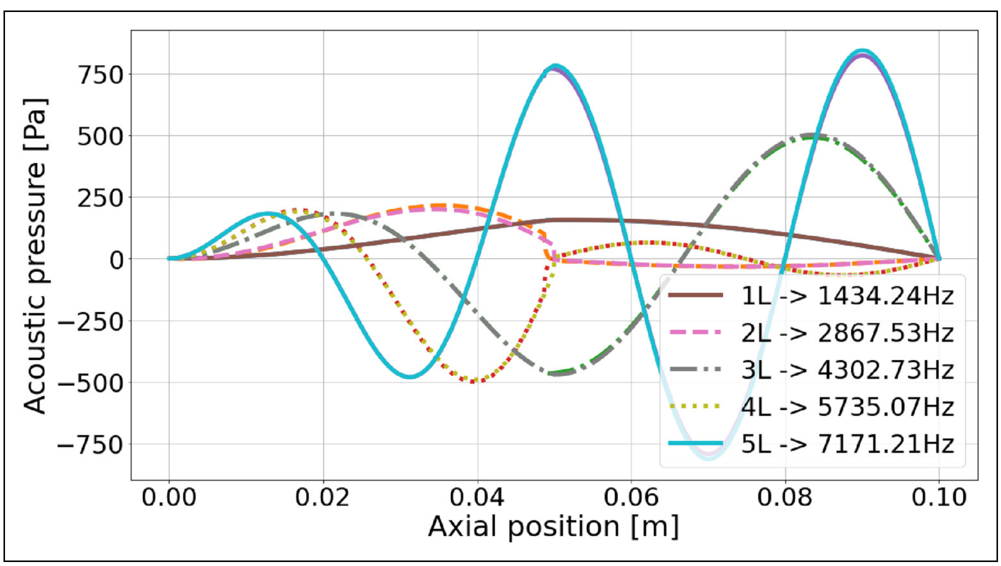

Figure 3. Modelling of a compact discontinuity between two straight tubes. Solution obtained with the state-of-the-art network element for a compact area discontinuity superimposed with that of the newly introduced one-dimensional (1D) isentropic model.

used to obtain the validation results. The software is not publicly available, but a complete description of the models is present in the Appendix.

The solution procedure is simple: once the desired model is chosen, it can be computed for a given frequency. Only for the resonant frequencies of the system will the longitudinal downstream BC be satisfied. Therefore, using a minimization algorithm the set of frequencies that satisfy said BC can be found. Other approaches, such as a sweep of values of the frequency are also valid, although might be more computationally demanding.

In order to perform the computation for a given frequency, the ODE of the given model need to be integrated. This can be done with any stiff ODE solver library. It is recommended to use a stiff or adaptive solver, as the gradients in the background flow of a rocket engine can be quite large.

Running the non-optimized Python code on a single thread on a regular desktop, the average computation time required to compute the longitudinal resonant frequencies of the system are of 15 minutes for the isentropic models and around 20 minutes for the flame model. To compute

Table 3. Resonant frequency comparison between experimental and acoustic simulations for BKD LP4.

	LORESA	Experiment	Error
L1	2851.67 + 362.52j	2951	3.37%
L2	5867.31 + 527.12j	5850	0.29%
T1	10178.01 + 167.18j	10220	0.41%
T1L1	11466.28 + 345.56j	11660	1.66%
T2	16195.05 + 88.03j	16680	2.91%
T2L1	19032.06 + 547.71j	–	–
T3	21601.12 + 43.38j	22780	5.18%
R1	19887.71 + 53.95j	20460	2.8%
R1L1	23033.39 + 287.50j	–	–

BKD: Brennkammer D; LORESA: Low-Order Rocket Engine Stability Analysis.

Table 4. Resonant frequency comparison between experimental and acoustic simulations for BKD LP3.

	LORESA	Experiment	Error
L1	2735.014 + 412.53j	2716	0.70%
L2	5660.03 + 517.76j	5533	2.30%
T1	9252.61 + 92.25j	9723	4.84%
T1L1	11684.43 + 502.42j	–	–
T2	14433.91 + 25.62j	15393	6.23%
T2L1	17921.81 + 271.23j	–	–
T3	19031.25 + 5.66e−05j	20892	8.90%
R1	17571.75 + 3.99j	–	–

BKD: Brennkammer D; LORESA: Low-Order Rocket Engine Stability Analysis.

the main longitudinal, tangential and radial resonant frequencies with the 3D flame model, the expected time is around 1 hour.

Experimental test cases

The described modelling environment was benchmarked with two published rocket combustor experiments of different scale and propellant combinations (liquid oxygen and hydrogen (LOX/H2) and liquid oxygen and natural gas/methane (LOX/NG)). Both combustion chambers showed operating conditions with stable combustion and unstable combustion.

Further information on the first combustor, Brennkammer D (BKD), can be found by Armbruster et al.,[46] Gröning et al.,[49] Armbruster et al.,[50] Gröning et al.[51] and Armbruster et al.[52,53] and previous studies about its stability behaviour include[4,9–12,15,54–57]

For the second combustor, Brenkammer N (BKN), information can be found by Martin et al.[45,58,59]

Results

In this section, the results obtained for two load points of the BKD engine and four load points of the BKN engine, computed using the new models implemented in the software 'LORESA' (Low-Order Rocket Engine Stability Analysis), are shown. In both cases, the results of the purely acoustic simulation (isentropic models) obtained with LORESA are presented first, followed by the stability analysis performed with LORESA using the novel distributed flame elements.

BKD

The background flow data for the following simulations of BKD was obtained from the work performed by Schulze.[11] The system is modelled using a single new isentropic element with an ideal closed BC at the inlet of the combustion chamber and the novel sonic BC at the throat of the nozzle.

Chamber acoustics. The values of the acoustic resonant frequencies computed with LORESA are compared to the experimental values obtained at DLR. The data for the so-called LP4 is shown in Table 3 and for LP3 in Table 4, respectively. The absolute error in the resonant frequencies obtained is between 0.29% and 5.18% and the mean error is 3.30%.

It is noted that LP3 presents slightly higher errors and that higher frequencies are typically predicted worse than low frequencies. It is also notable that the imaginary part representing the damping rate (negative growth rate) is positive for all the simulated frequencies. This is to be expected as the acoustic effect of the flame is not considered and, therefore, there are no excitation mechanisms.

Chamber stability. The stability of the chamber is studied using the newly developed distributed flame elements. The acoustic response of the flame is included, as well as its effect on the mean flow. The values of the boundary conditions are kept the same: closed at the inlet and the new sonic condition at the nozzle's throat.

Given that for both load points of BKD no experimentally-measured gain nor time lag were available, a sweep of possible values was first performed. Using said sweep, a set of 'stability maps' was generated, for which the stable and unstable combinations of gain and time lag were identified. In Figures 4 and 5, the stability maps for the T1 and R1 modes, respectively, of LP4 are presented and in Figures 6 and 7, for LP3. The white region represents the stable combinations, the rest of the regions represent the unstable configurations, with darker colours indicating a larger number of unstable modes appearing in the simulation.

It is observed that the stability maps for both load points show instability for given time lags even at low gains, while for other time lag values, the system is stable even for very

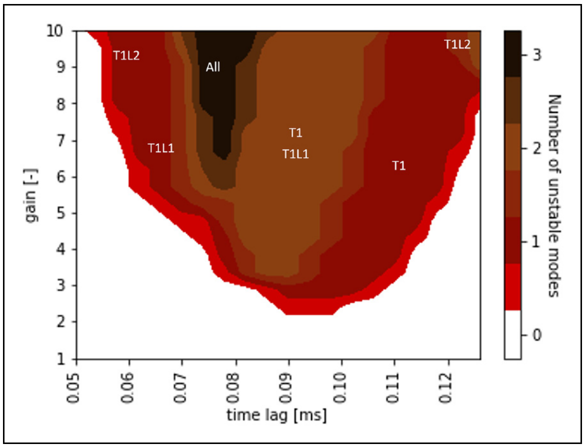

Figure 4. Stability map of Brennkammer D (BKD) LP4 T1Lx modes.

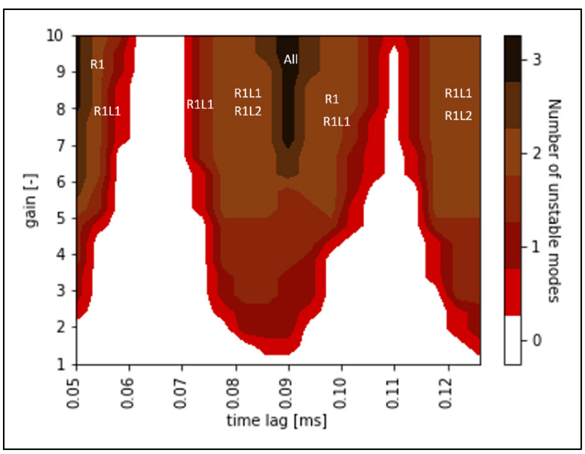

Figure 5. Stability map of Brennkammer D (BKD) LP4 R1Lx modes.

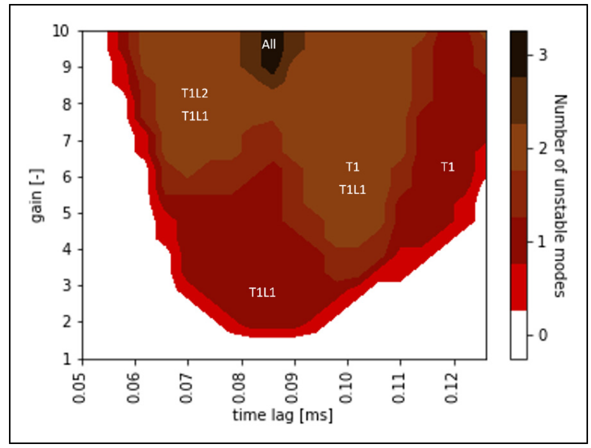

Figure 6. Stability map of Brennkammer D (BKD) LP3 T1Lx modes.

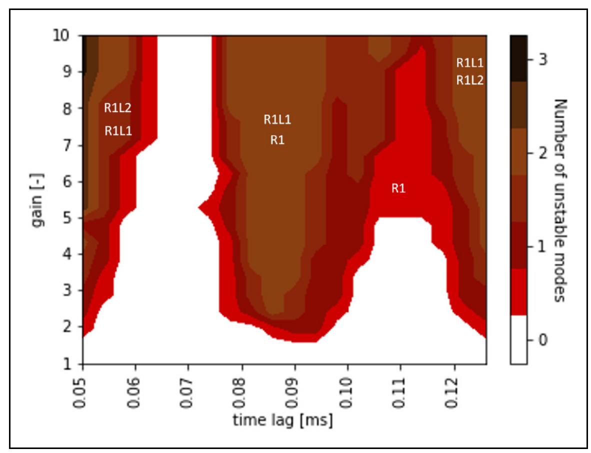

Figure 7. Stability map of Brennkammer D (BKD) LP3 R1Lx modes.

large gains. This can be easily related to the Rayleigh criterion. For some time, lags there is a strong coupling between the heat release and acoustic pressure, leading to instability even if the gain is low. On the other hand, other time lags are completely off-phase with the acoustic pressure, leading to stable configurations even for large gains.

For LP4, the experiment showed instability in the T1 mode. From experiment, it was found out that the R1 mode is also excited, but its amplitude is much less than the T1 mode. From the findings by Urbano and Selle,[55] it is known that the Rayleigh Index for the R1 mode is much smaller than that of the T1 mode. Furthermore, the T1 mode contributes significantly to the amplitude of the R1 mode. Thus, going to the stability map, we would expect to be at the limit between stable and unstable for the R1 mode (marginally unstable). Combining this with the clearly unstable T1, a gain around 3 and a time lag around 0.095 ms were estimated. Using these values resulted in a stable T1 mode for LP3 and an unstable T1 mode for LP4 (Table 5). For LP3, this gain and time lag also showed unstable T1L1 and R1L1 (Table 6). As the LP3 was stable, there might be some differences in the gain and time lag between LP3 and LP4 or some improvement to be made to the modelling. Nevertheless, the simulations correctly identified that the T1 mode was unstable for LP4 while stable for LP3.

Using these values of gain and time lag, the resonant frequencies were computed again. The results for LP3 are presented in Table 6 and for LP4 in Table 5. The average error of the resonant frequencies is 2.41%. There is a general decrease in this error as compared to the results of the purely acoustic approach. The largest errors are now found for the lower frequencies instead of the larger ones (specially in the LP3 L1 mode). It is considered that the larger errors in the longitudinal modes, when compared to the acoustic case, could be due to a necessity to introduce a

Table 5. Resonant frequency comparison between experimental and distributed flame simulations for BKD LP4.

	LORESA	Experimental	Error
L1	2971.70 + 252.65j	2951	0.70%
L2	5664.08 + 476.19j	5850	3.18%
T1	10561.71 − 39.76j	10220	3.34%
T1L1	11897.98 + 33.70j	11660	2.04%
T2	16887.43 + 379.88j	16680	1.24%
T2L1	17690.56 + 1432.07j	–	–
T3	22335.67 + 67.39j	22780	1.95%
R1	20683.09 + 62.74j	20460	1.09%
R1L1	22832.44 − 129.14j	–	–

BKD: Brennkammer D; LORESA: Low-Order Rocket Engine Stability Analysis.

Table 6. Resonant frequency comparison between experimental and distributed flame simulations for BKD LP3.

	LORESA	Experimental	Error
L1	2904.00 + 174.49j	2716	6.92%
L2	5418.83 + 373.05j	5533	2.06%
T1	9828.50 + 57.10j	9723	0.95%
T1L1	11550.18 − 129.86j	–	–
T2	15185.52 + 182.81j	15393	1.35%
T2L1	18671.65 + 309.67j	–	–
T3	20041.63 + 65.33j	20892	4.07%
R1	18547.80 + 109.26j	–	–

BKD: Brennkammer D; LORESA: Low-Order Rocket Engine Stability Analysis.

different dependence between unsteady heat release and acoustic pressure based on the mode under consideration, since tangential and longitudinal oscillations affect the combustion process differently. If this is true of longitudinal modes, it could explain why the T1L1 and R1L1 are wrongly predicted as unstable.

For both load points, experimental values for the damping rate of the T1 mode were computed by Schulze.[11] For LP3, damping was computed to be between 180 and 390 rad/s, while LORESA giving a lower value of 57 rad/s. For LP4, the damping ranges between −29 and −40 rad/s, with LORESA computing it at −40 rad/s. The damping seams to be underpredicted by LORESA, which is to be expected, as many of the effects leading to damping, such as a 3D background flow or viscosity were not accounted for.

BKN

The background flow data for the simulations of BKN was obtained from a radial average of a 3D RANS simulation performed at DLR. As this 3D RANS simulation was performed for a different chamber configuration than the one

Table 7. Longitudinal acoustic resonant frequencies comparison between simulation and experiment for BKN LP1 and LP2.

	LORESA	Experimental	Error
L1	823.33 + 67.42j	815 // 806	1.02% // 2.15%
L2	1653.12 + 82.89j	1625 // 1615	1.73% // 2.36%
L3	2488.84 + 90.30j	2448 // 2426	1.67% // 2.59%
L4	3329.33 + 87.40j	3257 // 3230	2.22% // 3.08%
L5	4172.43 + 77.41j	4077 // 4041	2.34% // 3.25%
L6	5015.32 + 72.02j	4889 // 4844	2.58% // 3.54%

BKN: Brenkammer N; LORESA: Low-Order Rocket Engine Stability Analysis.

Table 8. Longitudinal acoustic resonant frequencies comparison between simulation and experiment for BKN LP3.

	LORESA	Experimental	Error
L1	922.37 + 86.21j	920	0.26%
L2	1864.38 + 102.23j	1830	1.88%
L3	2817.53 + 90.53j	2758	2.16%
L4	3772.16 + 81.28j	3743	0.78%
L5	4727.10 + 90.29j	5679	1.03%

BKN: Brenkammer N; LORESA: Low-Order Rocket Engine Stability Analysis.

considered in this work, the data was scaled accordingly for each load point using the chamber and flame length. The system is modelled using a single new isentropic element with an ideal closed BC at the inlet of the combustion chamber and the novel sonic BC at the throat of the nozzle.

Chamber acoustics. The values of the acoustic resonant frequencies computed with LORESA are compared to the experimental values obtained by DLR. As LP1 and LP2 have the same chamber configuration and flame length, it results in the same scaling of the background flow. In consequence, they are treated as a single simulation case and compared with both experimental cases in Table 7. The comparison for LP3 is performed in Table 8 and for LP4 in Table 9. The mean error of the BKN simulations is 2.84%.

The results for LP4 are considerably worse than for the other cases, while LP1, 2, 3 have similar errors to BKD. It is believed that this might be caused by the background flow data scaling, as the flame length for LP4 case is unknown since it extended beyond the end of the window.

Once again, all the frequencies are predicted with positive damping rates and thus as stable since the excitation caused by the unsteady heat release is not included in this purely acoustic analysis.

Chamber stability. The stability of the chamber is studied using the newly developed distributed flame elements.

Table 9. Longitudinal acoustic resonant frequencies comparison between simulation and experiment for BKN LP4.

	LORESA	Experimental	Error
L1	893.81 + 99.80j	828	7.95%
L2	1829.96 + 80.00j	1728	5.9%
L3	2767.17 + 88.15j	2556	8.26%
L4	3685.54 + 93.86j	–	–
L5	4616.72 + 77.89j	–	–

BKN: Brenkammer N; LORESA: Low-Order Rocket Engine Stability Analysis.

Table 10. Experimental determined time lag values for the four BKN LPs.[60]

LP	P_{cc} (bar)	ROF	Time lag (ms)	Uncertainty
2,H_2	64.3	5.8	0.025	±0.05
1,CNG	66.8	2.8	0.1	±0.1
1,LNG	62.9	3.5	0.15	±0.05
2,LNG	65.4	3.0	0.12	±0.05
3,LNG	41.3	3.4	0.17	±0.1
4,LNG	40.5	2.5	0.2	±0.1

BKN: Brenkammer N; LP: load point; ROF: ratio of oxidizer to fuel; CNG: compressed natural gas; LNG: liquefied natural gas.

The acoustic response of the flame is included, as well as its effect on the mean flow.

For BKN, the time lag values for all four load points were experimentally measured[60] and provided in Table 10. As the gain is still unknown, the stability maps were once again generated via a sweep of various combinations of gain and time lag values. The stability map of the longitudinal modes for the short chamber (LP1 and LP2) is presented in Figure 8 and for the long chamber (LP3 and LP4) in Figure 9. Once again, the white region represents the stable combinations, the rest of the regions represent the unstable configurations, with darker colours indicating a larger number of unstable modes appearing in the simulation.

The first finding to be drawn, is that the lengthening of the chamber offsets the region of stability. The longer chamber (corresponding to LP3 and LP4) results in larger time lags needed for stability at high gains. As the length fundamentally changes the resonant frequency of the system, this once again shows that the code predicts coupling of the acoustic pressure and unsteady heat release based on the time lag value.

Using the stability maps and the experimentally measured values of the time lag, as well as the observed stability behaviour, an estimate of the gain can be obtained. Given that all four load points are relatively similar, a common gain value will be assumed. Since LP4 was at the boundary of stability (growth rate close to zero) and the other load points unstable, it is concluded that the gain should be close

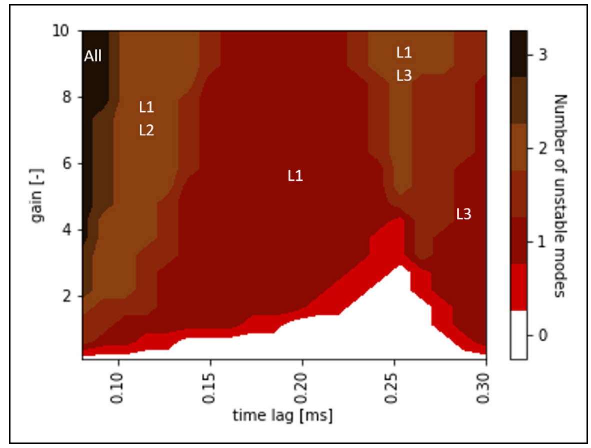

Figure 8. Stability map of Brenkammer N (BKN) short chamber Lx modes.

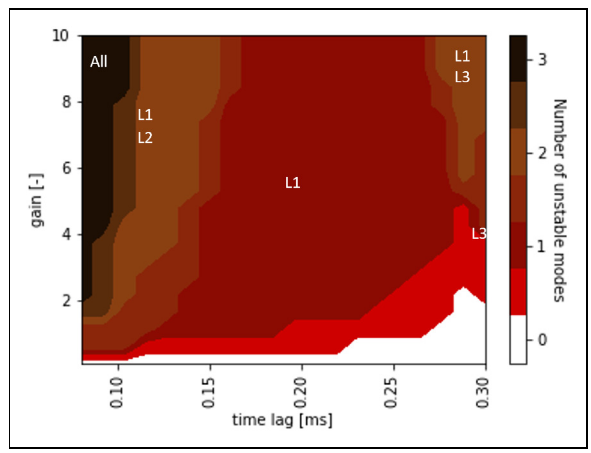

Figure 9. Stability map of Brenkammer N (BKN) long chamber Lx modes.

to 1. This gain results in matching stability between experiment and simulation.

Using the experimentally measured time lag values along with the gain values obtained from comparing the stability maps with the experimental observations, the four load points were once again simulated. The resonant frequencies computed using the distributed flame model are compared with their respective experimental measurements in Tables 11 to 14.

For the results of load points 1, 2 and 3, the imaginary part was not included. The resonant frequency was measured at the limit cycle at which, due to the longitudinal instability, there is a significant shortening of the flame. On the other hand, given the linear nature of the code, the stability prediction needs to be done at low amplitudes, while the acoustic oscillations are still small. Consequently, the flame length used for stability prediction is much larger than the one used to predict the resonant

Table 11. Longitudinal acoustic resonant frequencies comparison between distributed flame simulation and experiment for BKN LP1.

	LORESA	Experimental	Error
L1	781.41	815	4.12%
L2	1674.73	1625	3.06%
L3	2520.02	2448	2.94%
L4	3180.62	3257	2.35%
L5	4147.52	4077	1.73%
L6	4880.48	4889	0.17%

BKN: Brenkammer N; LORESA: Low-Order Rocket Engine Stability Analysis.

Table 12. Longitudinal acoustic resonant frequencies comparison between distributed flame simulation and experiment for BKN LP2.

	LORESA	Experimental	Error
L1	827.17	806	2.63%
L2	1669.99	1615	3.40%
L3	2454.50	2426	1.17%
L4	3410.55	3230	5.59%
L5	4232.78	4041	4.80%
L6	4978.41	4844	2.77%

BKN: Brenkammer N; LORESA: Low-Order Rocket Engine Stability Analysis.

frequency of the shorter flame configuration present at the limit cycle. Note that, for the longer flame (corresponding to the linear case), modes 1, 2 and 3 are correctly predicted as unstable, as shown in the stability maps, it is just for the shorter flame (corresponding to the behaviour at the limit cycle) where the damping rates are not correctly predicted.

The average error for all BKN simulations with distributed flame is 3.78%. This error is slightly larger than the one for the acoustic analysis. This could be related to the frequency being simulated with a linear tool but being measured at the limit cycle. Additionally, the distributed flame model generally exhibits larger errors on longitudinal modes than transverse modes.

Summary and conclusions

A set of new models for acoustic network elements have been developed which allow for a more accurate description of the acoustic field in rocket engine combustion chambers compared to the models highlighted in the state-of-the-art. The new models predict the acoustic resonant frequencies of the system for both longitudinal, tangential and radial modes as well as their stability. The models were implemented in an acoustic network environment tool called 'LORESA'. LORESA is capable of simulating both the injectors and combustion chamber including the convergent nozzle of a rocket engine.

Table 13. Longitudinal acoustic resonant frequencies comparison between distributed flame simulation and experiment for BKN LP3.

	LORESA	Experimental	Error
L1	854.58	920	7.11%
L2	1914.49	1830	4.62%
L3	2689.61	2758	2.48%
L4	3744.72	3743	0.05%
L5	4744.65	4679	1.40%

BKN: Brenkammer N; LORESA: Low-Order Rocket Engine Stability Analysis.

Table 14. Longitudinal acoustic resonant frequencies comparison between distributed flame simulation and experiment for BKN LP4.

	LORESA	Experimental	Error
L1	888.78 + 72.39j	828	7.34%
L2	1882.69 + 38.96j	1728	8.95%
L3	2782.50 + 56.51j	2556	8.86%

BKN: Brenkammer N; LORESA: Low-Order Rocket Engine Stability Analysis.

The most notable of the new elements is the distributed flame model, which can be used to predict the stability of the longitudinal, tangential and radial modes of a rocket engine combustion chamber. The model accounts for typical characteristics of cryogenic rocket combustion chambers, such as a long flame, non-isentropic behaviour and strong axial gradients in speed of sound and density.

The average error in the prediction of resonant frequencies obtained with the acoustic model was 3.4%. The errors for the predictions of the distributed flame model had an average of 3.56%. The stability of the main modes was correctly predicted for all the validation cases. The average error for the flame model was slightly higher than for the acoustic modelling. Nevertheless, for the cases in which most of the resonant frequencies were measured in the linear regime (BKD), the results proved to be much better for the stability modelling than for the purely acoustic modelling.

In conclusion, the newly developed models are able to give a stability prediction both for LOX/H2 and LOX/NG. The model also correctly differentiates the stability behaviour of two load points based on differences of inlet conditions or chamber length. The prediction of thermoacoustic resonant frequencies is achieved with low errors even across the different propellants and geometries tested. The linear stability analysis of the benchmarking test cases was successful, identifying values of gain and time lag that gave a correct stability behaviour across the different load points for each combustion chamber, matching their experimental behaviour.

ORCID iDs

Nicolas de Jong Cantarino https://orcid.org/0009-0000-0981-9694
Wolfgang Armbruster https://orcid.org/0000-0002-4859-4173
Justin Hardi https://orcid.org/0000-0003-3258-5261
Michael Börner https://orcid.org/0000-0002-3441-2869
Jan Martin https://orcid.org/0000-0002-5050-2506

Ethical considerations

No ethical approval was required.

Author contributions

WA: conceptualization; JH: resources; WA, JM and MB: data curation; NJC: software; NJC: formal analysis; WA and BZ: supervision; NJC and WA: investigation; NJC and WA: validation; NJC, WA and JM: original draft preparation; NJC, WA, JH and MB: review and editing; NJC and WA: visualization; WA, NJC, BZ and JH: project administration; JH: funding acquisition.

Funding

The authors received no external financial support for the research, authorship, and/or publication of this article.

Declaration of conflicting interest

The authors declared no potential conflicts of interest with respect to the research, authorship, and/or publication of this article

Data availability statement

The original contributions presented in this study are included in the article. Further inquiries can be directed to the corresponding authors.

References

1. Harrje D and Reardon F. *Liquid Propellant Rocket Combustion Instability*. NASA SP-194, 1972.
2. Yang V and Anderson W. *Liquid Rocket Engine Combustion Instability*. Washington, D.C.: American Institute of Aeronautics and Astronautics, 1995.
3. Hardi JS, Traudt T, Bombardieri C, et al. Combustion dynamics in cryogenic rocket engines: research programme at DLR Lampoldshausen. *Acta Astronaut* 2018; 147: 251–258.
4. Zolla P, Montanari A, Grossi M, et al. Low-order modeling of combustion instability: A comprehensive analysis of the BKD test case. In: *AIAA SCITECH 2024 Forum*. DOI: 10.2514/6.2024-0150.
5. Zhu Y, Liu F and Sirignano WA. Simulation of multi-injector H^2 -O_2 rocket combustion instability. In: *AIAA SCITECH 2025 Forum*. Orlando, FL: American Institute of Aeronautics and Astronautics. DOI: 10.2514/6.2025-0158.
6. Watanabe D, Manako H, Onga T, et al. Combustion stability improvement of LE-9 engine for booster stage of H3 launch vehicle. *Mitsub Heavy Indust Techn Rev* 2016; 53: 28–35.
7. Watanabe D, Nagasaki A, Negoro N, et al. Hot-fire testing of development booster engine for H3 launch vehicle. In: *Space propulsion conference 2016*. Rome, Italy.
8. Urbano A, Selle L, Staffelbach G, et al. Large eddy simulation of a model scale rocket engine. In: *9th Mediterranean combustion symposium*. Rhodos.
9. Urbano A, Selle L, Staffelbach G, et al. Exploration of combustion instability triggering using large eddy simulation of a multiple injector liquid rocket engine. *Combust Flame* 2016; 169: 129–140.
10. Urbano A, Douasbin Q, Selle L, et al. Study of flame response to transverse acoustic modes from the LES of a 42-injector rocket engine. *Proc Combust Inst* 2017; 36: 2633–2639.
11. Schulze M. *Linear Stability Assessment of Cryogenic Rocket Engines*. PhD Thesis, Technische Universität München, 2016.
12. Schmitt T, Staffelbach G, Ducruic S, et al. Large-eddy simulations of a sub-scale liquid rocket combustor: Influence of fuel injection temperature on thermo-acoustic stability. In: *7th European conference for aeronautics and aerospace sciences (EUCASS)*. Mailand. DOI: 10.13009/EUCASS 2017-352.
13. Sharma A, De A and Kumar SS. Numerical investigation of supercritical combustion dynamics in a multi-element LOX–methane combustor using flamelet-generated manifold approach. *Phys Fluids* 2023; 35: 115125.
14. Schmitt T, Staffelbach G, Ducruix S, et al. Large-eddy simulations of a sub-scale liquid rocket combustor: influence of fuel injection temperature on thermo-acoustic stability. In: *7th European conference for aeronautics and aerospace sciences (EUCASS)*. Milan, Italy.
15. Schmitt T and Staffelbach G. REST HF-9 test case: Large-eddy simulation of DLR's BKD configuration. In: *9th European conference for aeronautics and aerospace sciences (EUCASS)*. Lille, France.
16. Poinsot T. *Theoretical and Numerical Combustion*. Edwards, 2001.
17. Polifke W, van der Hoek J and Verhaar B. *Everything You Always Wanted to Know about F and G*. Technische Universität München, 1997.
18. Huber W. *Impact of Fuel Supply Impedance on Combustion Stability of Gas Turbines*. PhD Thesis, Technische Universität München, 2009.
19. Palies P, Durox D, Schuller T, et al. Nonlinear combustion instability analysis based on the flame describing function applied to turbulent premixed swirling flames. *Combust Flame* 2011.
20. Gröning S. *Untersuchung selbsterregter Verbrennungsinstabilitäten in einer Raketenbrennkammer*. PhD Thesis, RWTH Aachen, 2017.
21. Armbruster W, Hardi JS, Suslov D, et al. Experimental investigation of self-excited combustion instabilities with

injection coupling in a cryogenic rocket combustor. *Acta Astronaut* 2018; 151: 655–667.
22. Karthik B, Kumar BM and Sujith RI. Exact solutions to one-dimensional acoustic fields with temperature gradient and mean flow. *J Acoust Soc Am* 2000; 108: 38–43.
23. Sujith RI, Waldherr GA and Zinn B. An exact solution for one-dimensional acoustic fields in duct with an axial temperature gradient. *J Sound Vib* 1995; 184: 389–402.
24. Li J and Morgans AS. The one-dimensional acoustic field in a duct with arbitrary mean axial temperature gradient and mean flow. *J Sound Vib* 2017; 400: 248–269.
25. Nicoud F and Wieczorek K. About the zero Mach number assumption in the calculation of thermoacoustic instabilities. *Int J Spray Combust Dynam* 2009; 1: 67–111.
26. Schaefer F and Polifke W. Low-order network modeling of a duct with non-uniform cross-section and arbitrary mean temperature gradient in the presence of mean flow. In: *AIAA propulsion and energy 2019 Forum*. American Institute of Aeronautics and Astronautics. DOI: 10.2514/6.2019-4376.
27. Cummings A. Ducts with axial temperature gradients: An approximate solution for sound transmission and generation. *J Sound Vib* 1977; 51: 55–67.
28. Davies POAL. Plane wave reflection at flow intakes. *J Sound Vib* 1987; 115: 560–564.
29. Davies POAL. Practical flow duct acoustics. *J Sound Vib* 1988; 124: 91–115.
30. Marble SMCandel FE. Acoustic disturbance from gas non-uniformities convected through a nozzle. *J Sound Vib* 1977; 55: 225–243.
31. Duran I and Moreau S. Solution of the quasi-one-dimensional linearized Euler equations using flow invariants and the Magnus expansion. *J Fluid Mech* 2013; 723: 190–231.
32. Li J, Yang D, Luzzato C, et al. Open source combustion instability low order simulator. *Imperial Coll London, London* 2017; 1–48.
33. Han X, Li J and Morgans AS. Prediction of combustion instability limit cycle oscillations by combining flame describing function simulations with thermoacoustic network model. *Combust Flame* 2015; 162: 3632–3647.
34. Software package tax. https://www.epc.ed.tum.de/en/tfd/research/tax-software/ (accessed: 29 November 2023).
35. Ekici E, Falco S and Juniper MP. Helmholtz-x: Parallelized adjoint open source solver for the thermoacoustic Helmholtz equation. *Eng Comput* 2025; 41: 2137–2164.
36. Cantwell C, Moxey D, Comerford A, et al. Nektar++: An open-source spectral/hp element framework. *Comput Phys Commun* 2015; 192: 205–219.
37. Moxey D, Cantwell CD, Bao Y, et al. Nektar++: Enhancing the capability and application of high-fidelity spectral/hp element methods. *Comput Phys Commun* 2020; 249: 107110.
38. Crocco L. Research on combustion instabilities in liquid propellant rockets. *12th Symp (Int) Combust* 1969: 4–6.
39. Polifke W. Modeling and analysis of premixed flame dynamics by means of distributed time delays. *Prog Energy Combust Sci* 2020; 79.
40. Casiano MJ. Extensions to the time lag models for practical application to rocket engine stability design. 2010.
41. Polifke W. Combustion instabilities. *Adv Aeroacoust Appl* 2004; 5.
42. Polifke W, Poncet A, Paschereit CO, et al. Reconstruction of acoustic transfer matrices by instationary computational fluid dynamics. *J Sound Vib* 2001: 5–9.
43. Schuermans B, Güthe F, Pennell D, et al. Thermoacoustic modeling of a gas turbine using transfer functions measured under full engine pressure. *J Eng Gas Turbines Power-Trans The Asme - J ENG GAS TURB POWER-T ASME* 2010; 132: 3–5. DOI: 10.1115/1.4000854.
44. Bothien M, Moeck JP, Lacarelle A, et al. Time domain modelling and stability analysis of complex thermoacoustic systems. *Proc Inst Mech Eng Part A: J Power Energy* 2007; 221: 657–668.
45. Martin J, Armbruster W, Börner M, et al. Flame-acoustic interaction in a high-pressure, single-injector, LOX/CNG rocket combustor with optical access. In: *AIAA SCITECH 2023 Forum*. American Institute of Aeronautics and Astronautics. DOI: 10.2514/6.2023-1838.
46. Armbruster W, Hardi JS and Oschwald M. REST HF-7 and HF-9 test case: Lessons learned for comparing simulation results with test data of a representative LOX/H2 thrust chamber with high-frequency combustion instabilities. In: *9th European conference for aeronautics and aerospace sciences (EUCASS)*. Lille, France.
47. Martin J, Armbruster W, Stützer R, et al. Flame characteristics of a high-pressure LOX/H2 rocket combustor with large optical access. *Case Stud Thermal Eng* 2021; 28: 101546.
48. Schulze M, Gikadi J and Sattelmayer T. Acoustic admittance prediction of two nozzle designs of different length using frequency domain simulations. In: *5th European conference for aeronautics and space sciences (EUCASS)*. München.
49. Gröning S, Hardi JS, Suslov D, et al. Injector-driven combustion instabilities in a hydrogen/oxygen rocket combustor. *J Propul Power* 2016; 32: 560–573.
50. Armbruster W, Hardi JS, Suslov D, et al. Injector-driven flame dynamics in a high-pressure multi-element oxygen-hydrogen rocket thrust chamber. *J Prop Power* 2019; 35: 632–644.
51. Gröning S, Hardi JS, Suslov D, et al. Influence of hydrogen temperature on the stability of a rocket engine combustor operated with hydrogen and oxygen. *CEAS Space J* 2017; 9: 59–76.
52. Armbruster W, Hardi JS and Oschwald M. Flame-acoustic response measurements in a high-pressure, 42-injector, cryogenic rocket thrust chamber. *Proc Combust Inst* 2020. 10.1016/j.proci.2020.05.020.
53. Armbruster W, Hardi J and Oschwald M. Impact of shear-coaxial injector hydrodynamics on high-frequency combustion instabilities in a representative cryogenic rocket engine. *Int J Spray Combust Dyn* 2022; 14: 118–130.
54. Schulze M and Sattelmayer T. Linear stability assessment of a cryogenic rocket engine. *Int J Spray Combust Dyn* 2017; 9: 277–298.

55. Urbano A and Selle L. Driving and damping mechanisms for transverse combustion instabilities in liquid rocket engines. *J Fluid Mech* 2017; 820. DOI: 10.1017/jfm.2017.227.
56. Hardi JS, Kaess R, Tonti F, et al. Study of the influence of operating conditions on LOx/H2 thrust chamber acoustic eigenmodes. In: *Space propulsion conference*, 2018. Sevilla, Spain.
57. Hwang WS, Sung BK, Han W, et al. Real-gas-flamelet-model-based numerical simulation and combustion instability analysis of a GH2/LOX rocket combustor with multiple injectors. *Energies* 2021; 14: 419.
58. Martin J, Armbruster W, Stützer R, et al. Flame dynamics of an injection element operated with LOX/H2, LOX/CNG and LOX/LNG in a sub- and supercritical rocket combustor with large optical access. *Int J Spray Combust Dyn* 2023; 15: 147–165.
59. Martin J, Armbruster W, Börner M, et al. Influence of injector and chamber geometry on the thermoacoustic behaviour in proximity to the stability boundary of LOX/CH4 rocket combustors. In: *AIAA SCITECH 2025 Forum*. American Institute of Aeronautics and Astronautics. DOI: 10.2514/6.2025-1549.
60. Martin J, Armbruster W, Börner M, et al. Flame response of a sub- and supercritical LOX/H2 and LOX/LNG rocket combustor with large optical access. *J Evolv Space Activ* 2025; 3: 225.

Appendix

Full derivation of 1D isentropic acoustics with area variation. Under the assumptions of no heat transfer, no viscosity or losses, no body forces and no chemical reactions, the resulting continuity, momentum and energy equations read:

$$A\frac{D\rho}{Dt}+\rho\frac{\partial(uA)}{\partial x}=0 \tag{23}$$

$$\rho\frac{\partial u}{\partial t}+\rho u\frac{\partial u}{\partial x}+\frac{\partial p}{\partial x}=0 \tag{24}$$

$$\rho T\frac{DS}{Dt}=0 \tag{25}$$

In order to model the acoustics, it will be considered that pressure, density and velocity have a 'background flow' component and an 'acoustics' component, where the acoustic component is small in comparison with the background flow value. Consequently, these variables can be expressed as shown in equation (26). Furthermore, all background variables are purely a function of the longitudinal variable, explicitly written in equation (27).

$$\begin{gathered}p=p_0+\hat{p}(t,x),\quad \rho=\rho_0+\hat{\rho}(t,x),\\ u=u_0+\hat{u}(t,x),\quad c=c_0+\hat{c}(x,t)\end{gathered} \tag{26}$$

$$\begin{gathered}u_0\equiv u_o(x),\quad p_0\equiv p_0(x),\quad \rho_0\equiv\rho_0(x),\\ c_0\equiv c_0(x),\quad A\equiv A(x),\quad M(x)=\frac{u_0(x)}{c_0(x)}\end{gathered} \tag{27}$$

Since the substantial derivative (denoted with a capital D) of the entropy is zero, for a perfect gas it follows that the substantial derivative of the pressure is proportional to the substantial derivative of density, as shown in equation (28). If we consider zero temporal derivatives of entropy, we can further simplify the expression and linearization a simple relation between acoustic density and pressure is obtained, as shown in equation (29).

$$\begin{gathered}dS=\left(\frac{\partial S}{\partial p}\right)_\rho dp+\left(\frac{\partial S}{\partial \rho}\right)_p d\rho \quad\rightarrow\\ 0=\frac{Dp}{Dt}+\frac{\left(\frac{\partial S}{\partial \rho}\right)_p}{\left(\frac{\partial S}{\partial p}\right)_\rho}\frac{D\rho}{Dt}\quad\rightarrow\quad \frac{Dp}{Dt}=c^2\frac{D\rho}{Dt}\end{gathered} \tag{28}$$

$$\frac{dp}{dt}=c^2\frac{d\rho}{dt}\quad\rightarrow\quad\frac{d\hat{p}}{dt}=c_0^2\frac{d\hat{\rho}}{dt}\quad\rightarrow\quad\hat{p}=c_0^2\hat{\rho} \tag{29}$$

Equation (28) is used in the continuity equation to substitute the density derivatives. Then, equations (26) and (27) are substituted into equations (23) and (24). The background flow already satisfies the equations and that the acoustics are linearized (products of two or more acoustic variables are removed from the equations). Afterwards, equation (29) is used to substitute the acoustic density. The resulting expressions are shown subsequently:

$$\begin{aligned}&\frac{A}{c_0^2}\frac{\partial\hat{p}}{\partial t}+\frac{u_0A}{c_0^2}\frac{\partial\hat{p}}{\partial x}+A\frac{\hat{p}}{c_0^2}\frac{\partial u_0}{\partial x}+u_0\frac{\hat{p}}{c_0^2}\frac{\partial A}{\partial x}\\ &\quad+\dot{m}\left(\frac{1}{u_0}\frac{\partial\hat{u}}{\partial x}-\frac{\hat{u}}{u_0^2}\frac{\partial u_0}{\partial x}\right)=0\end{aligned} \tag{30}$$

$$\rho_0\frac{\partial\hat{u}}{\partial t}+\rho_0u_0\frac{\partial\hat{u}}{\partial x}+\rho_0\hat{u}\frac{\partial u_0}{\partial x}+\hat{p}\frac{u_0}{c_0^2}\frac{\partial u_0}{\partial x}+\frac{\partial\hat{p}}{\partial x}=0 \tag{31}$$

Note that the relation $\partial(\rho_0u_0A)/\partial x=0$ has been used to remove the derivatives of the background density, this will be done repeatedly in the following steps. Reorganizing the previous relations, equations (32) and (33) are obtained.

$$\begin{aligned}&\frac{1}{\rho_0c_0}\left(\frac{1}{c_0}\frac{\partial}{\partial t}+M_0\frac{\partial}{\partial x}+M\frac{1}{A}\frac{\partial A}{\partial x}+M\frac{1}{u_0}\frac{\partial u_0}{\partial x}\right)\hat{p}\\ &\quad+\left(\frac{\partial}{\partial x}-\frac{1}{u_0}\frac{\partial u_0}{\partial x}\right)\hat{u}=0\end{aligned} \tag{32}$$

$$\begin{aligned}&\left(\frac{1}{c_0}\frac{\partial}{\partial t}+M\frac{\partial}{\partial x}+M\frac{1}{u_0}\frac{\partial u_0}{\partial x}\right)\hat{u}\\ &\quad+\frac{1}{\rho_0c_0}\left(M^2\frac{1}{u_0}\frac{\partial u_0}{\partial x}+\frac{\partial}{\partial x}\right)\hat{p}=0\end{aligned} \tag{33}$$

Since these two equations do not have an analytical solution, the shape of the acoustic pressure and velocity will be assumed, as shown in equations (34) and (35). This assumptions are made based on the analytical solution for 1D acoustics with constant incompressible background flow.

It is assumed that the exponents for the pressure and velocity are different, as well as their coefficients. It is shown next that either only the exponents or only the coefficients need to differ. Moreover, a notation change is included to simplify the equations, shown in equation (36).

$$\hat{p} = \rho_0 c_0 \cdot \mathcal{R}e\left(e^{i\omega t}\left[f_p e^{-ik_{f,p}(x)} + g_p e^{-ik_{g,p}(x)}\right]\right) \tag{34}$$

$$\hat{u} = \mathcal{R}e\left(e^{i\omega t}\left[f_u e^{-ik_{f,u}(x)} + g_u e^{-ik_{g,u}(x)}\right]\right) \tag{35}$$

$$\frac{1}{a}\frac{\partial a}{\partial x} \equiv \frac{\partial a}{a} \tag{36}$$

It should also be noted that the derivative of the acoustic pressure with respect to the longitudinal coordinate is not as trivial as that of the velocity or the incompressible case, as the acoustic pressure is function of the density and speed of sound which also vary with the axial coordinate. Consequently, the derivative must be taken with care, as shown in equation (37).

$$\begin{aligned}\frac{1}{\rho_0 c_0}\frac{\partial \hat{p}}{\partial x} &= \frac{1}{\rho_0 c_0}\frac{\partial(\rho_0 c_0)}{\partial x} + \frac{\partial(\hat{p}/(\rho_0 c_0))}{\partial x} \\ &= \left(\frac{\partial \rho_0}{\rho_0} + \frac{\partial c_0}{c_0} - i\frac{\partial k_p}{\partial x}\right)\frac{\hat{p}}{\rho_0 c_0}\end{aligned} \tag{37}$$

Note that for the variable k_p represents both $k_{f,p}$ and $k_{g,p}$. The subindexes f and g have been dropped for convenience, as the equation is the same in both cases. This notation simplification is done throughout the Appendix, as long as the only difference between the equations for f and g reside in the variable being used (note that $k_{f,p} \neq k_{g,p}$). Performing the acoustic pressure derivatives in equations (32) and (33) and substituting the values of the acoustic pressure and velocity given in equations (34) and (35) a set of four equations is obtained, shown in equations (38) and (39). Given that each equation needs to be verified independently for the forward and backward waves (as both should be solutions of the system), the resulting system consists of two continuity equations and two momentum equations (one for f_p, $k_{f,p}$, f_u, and $k_{f,u}$ and another for g_p, $k_{g,p}$, g_u and $k_{g,u}$).

$$\begin{aligned}&\left(\frac{i\omega}{c_0} + M_0\frac{\partial c_0}{c_0} - iM_0\frac{\partial k_p}{\partial x}\right)\begin{bmatrix} f_p \\ g_p \end{bmatrix} e^{-ik_p} \\ &= \left(\frac{\partial u_0}{u_0} + i\frac{\partial k_u}{\partial x}\right)\begin{bmatrix} f_u \\ g_u \end{bmatrix} e^{-ik_u}\end{aligned} \tag{38}$$

$$\begin{aligned}&\left((M_0^2 - 1)\frac{\partial u_0}{u_0} + \frac{\partial c_0}{c_0} - \frac{\partial A}{A} - i\frac{\partial k_p}{\partial x}\right)\begin{bmatrix} f_p \\ g_p \end{bmatrix} e^{-ik_p} \\ &= \left(-\frac{i\omega}{c_0} + iM_0\frac{\partial k_u}{\partial x} - M_0\frac{\partial u_0}{u_0}\right)\begin{bmatrix} f_u \\ g_u \end{bmatrix} e^{-ik_u}\end{aligned} \tag{39}$$

It should be noted that any difference between the coefficients of the pressure and velocity could be 'absorbed' into the exponents, as any complex number can be represented as the exponent of a different complex number and the product of exponential corresponds to the addition of the exponents. Consequently, it would be useful to use the same f and g for pressure and velocity ($f_p = f_u$ and $g_p = g_u$) and have the exponents be different to represent the compressibility effects. To simplify notation, two new variables have been introduced, that represent the difference between the pressure and velocity exponents, as shown in equations (40) and (41). The negative sign for η_g has been introduced in order to have equivalent notation to the uniform flow case, where $g_p = -g_u$.

$$\eta_f(x) = e^{-i\left(k_{f,u}(x) - k_{f,p}(x)\right)} \tag{40}$$

$$\eta_g(x) = -e^{-i\left(k_{g,u}(x) - k_{g,p}(x)\right)} \tag{41}$$

Applying this in equations (38) and (39), four new equations can be obtained, shown in equations (42) and (43).

$$\begin{cases} \frac{i\omega}{c_0} + M_0\frac{\partial c_0}{c_0} - iM_0\frac{\partial k_{f,p}}{\partial x} = \left(\frac{\partial u_0}{u_0} + i\frac{\partial k_{f,u}}{\partial x}\right)\eta_f \\ \left(M_0^2 - 1\right)\frac{\partial u_0}{u_0} + \frac{\partial c_0}{c_0} - \frac{\partial A}{A} - i\frac{\partial k_{f,p}}{\partial x} = \left(-\frac{i\omega}{c_0} + iM_0\frac{\partial k_{f,u}}{\partial x} - M_0\frac{\partial u_0}{u_0}\right)\eta_f \end{cases} \tag{42}$$

$$\begin{cases} \frac{i\omega}{c_0} + M_0\frac{\partial c_0}{c_0} - iM_0\frac{\partial k_{g,p}}{\partial x} = \left(\frac{\partial u_0}{u_0} + i\frac{\partial k_{g,u}}{\partial x}\right)\eta_g \\ \left(M_0^2 - 1\right)\frac{\partial u_0}{u_0} + \frac{\partial c_0}{c_0} - \frac{\partial A}{A} - i\frac{\partial k_{g,p}}{\partial x} = \left(-\frac{i\omega}{c_0} + iM_0\frac{\partial k_{g,u}}{\partial x} - M_0\frac{\partial u_0}{u_0}\right)\eta_g \end{cases} \tag{43}$$

The reader can check that, if all gradients of background flow and area are removed, the set of equations leads to $k_u = k_p$ and solving it yields the solution for the duct with uniform flow. On the other hand, for the case under consideration, it is required that $k_u \neq k_p$ in order to obtain a valid solution. This system of four differential equations contains four unknowns (the four wave numbers: $k_{f,p}$, $k_{f,u}$, $k_{g,p}$ and $k_{g,u}$) and only order one derivatives, consequently it can be simply solved by a stiff ODE solver. To facilitate this task the system will be re-arranged into a more useful shape:

$$\begin{aligned} i\left(1 - M_0^2\right)\frac{\partial k_{f,p}}{\partial x} = &\left(M_0^2 + 2M_0\eta_f - 1\right)\frac{\partial u_0}{u_0} \\ &+ \left(1 - M_0^2\right)\frac{\partial c_0}{c_0} - \frac{\partial A}{A} \\ &+ \left(\eta_f - M_0\right)\frac{i\omega}{c_0} \end{aligned} \tag{44}$$

$$\begin{aligned} i\frac{\partial k_{f,u}}{\partial x} = &\left(\frac{M_0}{\eta_f} - \frac{2}{1 - M_0^2} + 1\right)\frac{\partial u_0}{u_0} + \frac{1}{\eta_f}\frac{M_0}{1 - M_0^2}\frac{\partial A}{A} \\ &+ \frac{1}{M_0}\left(1 - \frac{1}{\eta_f}\frac{\eta_f - M_0}{1 - M_0^2}\right)\frac{i\omega}{c_0} \end{aligned} \tag{45}$$

The equations for $k_{g,p}$, $k_{g,u}$ are identical to the ones for $k_{f,p}$, $k_{f,u}$ but substituting η_f for η_g. The upstream boundary conditions for the exponents are all 0, reasoning that in the incompressible case for $x = 0$ the exponents were also 0, as the constant k value multiplied the x coordinate. It is also assumed that the initial value of the coefficients is that of the incompressible case (already accounted for in the presented set of equations). Therefore,

$$\begin{aligned} k_{f,p}(0) = 0, \quad k_{f,u}(0) = 0, \quad k_{g,p}(0) = 0, \\ k_{g,u}(0) = 0, \quad \eta_f(0) = 1, \quad \eta_g(0) = -1 \end{aligned} \tag{46}$$

Consequently, even if the equations for $k_{g,p}$, $k_{g,u}$ have the same structure as for $k_{f,p}$, $k_{f,u}$, the difference in upstream boundary conditions between η_f and η_g results in a different solution. Once again, removing all gradients of background flow and area and using these upstream boundary conditions, the solution for the uniform flow duct is obtained, where $k_{f,p} = k_{f,u} = \frac{\omega/c_0}{1+M_0}$ and $k_{g,p} = k_{g,u} = \frac{-\omega/c_0}{1-M_0}$.

Full derivation of 3D isentropic acoustics. Under the same hypothesis of the 1D case, the resulting 3D equations of continuity and momentum are as follows:

$$\frac{\partial \rho}{\partial t} + \frac{1}{r}\left(\frac{\partial(\rho r u_r)}{\partial r} + \frac{\partial(\rho u_\theta)}{\partial \theta} + \frac{\partial(\rho r u_z)}{\partial z}\right) = 0 \tag{47}$$

$$\rho\left(\frac{\partial u_r}{\partial t} + u_r\frac{\partial u_r}{\partial r} + \frac{u_\theta}{r}\frac{\partial u_r}{\partial \theta} + u_z\frac{\partial u_r}{\partial z} - \frac{u_\theta^2}{r}\right) = -\frac{\partial p}{\partial r} \tag{48}$$

$$\begin{aligned} &\rho\left(\frac{\partial u_\theta}{\partial t} + u_r\frac{\partial u_\theta}{\partial r} + \frac{u_\theta}{r}\frac{\partial u_\theta}{\partial \theta} + u_z\frac{\partial u_\theta}{\partial z} - \frac{u_\theta u_r}{r}\right) \\ &\quad = -\frac{1}{r}\frac{\partial p}{\partial \theta} \end{aligned} \tag{49}$$

$$\rho\left(\frac{\partial u_z}{\partial t} + u_r\frac{\partial u_z}{\partial r} + \frac{u_\theta}{r}\frac{\partial u_z}{\partial \theta} + u_z\frac{\partial u_z}{\partial z}\right) = -\frac{\partial p}{\partial z} \tag{50}$$

The same assumption is made regarding the variables being composed of a 'background flow' and an 'acoustic' component, as shown in equation (51), including the dependency with the other two spatial coordinates. The background flow is given by equation (52), where the fluidic variables are now a function exclusively of the axial variable but the tangential and radial velocities are zero. Although the final result will only be valid for a constant area tube, the area is initially considered a function of the axial coordinate to show why the 3D incompressible element with varying area cannot be obtained through this method.

$$\begin{aligned} p = p_0 + \hat{p}(t, r, \theta, z), \quad \rho = \rho_0 + \hat{\rho}(t, r, \theta, z), \\ u = u_0 + \hat{u}(t, r, \theta, z), \quad c = c_0 + \hat{c}(t, r, \theta, z) \end{aligned} \tag{51}$$

$$\begin{aligned} u_{r,0} = 0, \quad u_{\theta,0} = 0, \quad u_{z,0} \equiv u_{z,0}(z), \quad p_0 \equiv p_0(z), \\ \rho_0 \equiv \rho_0(z), \quad c_0 \equiv c_0(z), \quad A \equiv A(z) \end{aligned} \tag{52}$$

Substituting said values into the continuity and momentum equations, removing the terms function only of the background flow (as it is a solution to the equations) and linearizing the acoustics (removing products of two or more acoustic variables), the following relations are obtained:

$$\frac{\partial \hat{\rho}}{\partial t} + \frac{1}{r}\left(\frac{\partial(\rho_0 r \hat{u}_r)}{\partial r} + \frac{\partial(\rho_0 \hat{u}_\theta)}{\partial \theta} + \frac{\partial(\rho_0 r \hat{u}_z)}{\partial z} + \frac{\partial(\hat{\rho} r u_{z,0})}{\partial z}\right) = 0 \tag{53}$$

$$\rho_0\left(\frac{\partial \hat{u}_r}{\partial t} + u_{z,0}\frac{\partial \hat{u}_r}{\partial z}\right) = -\frac{\partial \hat{p}}{\partial r} \tag{54}$$

$$\rho_0\left(\frac{\partial \hat{u}_\theta}{\partial t} + u_{z,0}\frac{\partial \hat{u}_\theta}{\partial z}\right) = -\frac{1}{r}\frac{\partial \hat{p}}{\partial \theta} \tag{55}$$

$$\rho_0\left(\frac{\partial \hat{u}_z}{\partial t} + u_{z,0}\frac{\partial \hat{u}_z}{\partial z} + \hat{u}_z\frac{\partial u_{z,0}}{\partial z}\right) + \hat{\rho} u_{z,0}\frac{\partial u_{z,0}}{\partial z} = -\frac{\partial \hat{p}}{\partial z} \tag{56}$$

The previous equations are re-arranged and the acoustic density is substituted by the pressure using the relationship shown in the 1D case ($\hat{\rho} = \frac{\hat{p}}{c_0^2}$). This relationship is still valid since the same assumptions also lead to an isentropic flow in the 3D case. The following set of four equations is obtained:

$$\begin{aligned} &\frac{1}{\rho_0 c_0}\left(\frac{1}{c_0}\frac{\partial}{\partial t} + M_{z,0}\frac{\partial}{\partial z} - 2M_{z,0}\frac{1}{c_0}\frac{\partial c_0}{\partial z} + M_{z,0}\frac{1}{u_{z,0}}\frac{\partial u_{z,0}}{\partial z}\right)\hat{p} \\ &\quad + \left(\frac{\partial}{\partial r} + \frac{1}{r}\right)\hat{u}_r + \frac{1}{r}\frac{\partial \hat{u}_\theta}{\partial \theta} + \left(\frac{\partial}{\partial z} + \frac{1}{\rho_0}\frac{\partial \rho_0}{\partial z}\right)\hat{u}_z \\ &\quad = 0 \end{aligned} \tag{57}$$

$$\frac{1}{c_0}\frac{\partial \hat{u}_r}{\partial t} + M_{z,0}\frac{\partial \hat{u}_r}{\partial z} = -\frac{\partial(\hat{p}/(\rho_0 c_0))}{\partial r} \tag{58}$$

$$\frac{1}{c_0}\frac{\partial \hat{u}_\theta}{\partial t} + M_{z,0}\frac{\partial \hat{u}_\theta}{\partial z} = -\frac{1}{r}\frac{\partial(\hat{p}/(\rho_0 c_0))}{\partial \theta} \tag{59}$$

$$\begin{aligned} &\frac{1}{c_0}\frac{\partial \hat{u}_z}{\partial t} + M_{z,0}\frac{\partial \hat{u}_z}{\partial z} + M_{z,0}\frac{1}{u_{z,0}}\frac{\partial u_{z,0}}{\partial z}\hat{u}_z \\ &\quad = -\frac{1}{\rho_0 c_0}\left(M_{z,0}^2\frac{1}{u_{z,0}}\frac{\partial u_{z,0}}{\partial z} + \frac{\partial}{\partial z}\right)\hat{p} \end{aligned} \tag{60}$$

Once again, as no analytical solution exists for this set of equations, the shape of the solutions will need to be assumed to aid the resolution process. The shape of the acoustic variables will be assumed to be that of the analytical case (with the exception of the correction coefficients of the axial velocity being absorbed into its exponent, much like in the 1D case). The shape of the acoustic variables is presented in equations (61) to (64), where J_n represents the Bessel function of the first kind of order n (which will be crucial later on in the derivation) and $\beta_{m,n}$ corresponds to the mth zero of the derivative of the Bessel function of the first kind of order n. This expressions have already accounted for the radial and tangential boundary conditions: zero radial velocity at the walls, finite radial velocity at the axis and continuity of the tangential velocity and its derivative. The application of these BCs has not been shown as it is identical to the process carried out for the incompressible 3D duct.

$$\frac{\hat{p}}{\rho_0 c_0}(z, r, \theta, t) = J_n\left(\pi\beta_{m,n}\frac{r}{R}\right)\mathcal{R}e \left[\left(fe^{-ik_{f,p}(z)} + ge^{-ik_{g,p}(z)}\right)\left(Pe^{-in\theta} + Qe^{in\theta}\right)e^{i\omega t}\right] \quad (61)$$

$$\hat{u}_r(z, r, \theta, t) = \frac{\partial J_n\left(\pi\beta_{m,n}\frac{r}{R}\right)}{\partial r}\mathcal{R}e \left[\left(\eta_{r,f}fe^{-ik_{f,p}(z)} + \eta_{r,g}ge^{-ik_{g,p}(z)}\right)\left(Pe^{-in\theta} + Qe^{in\theta}\right)e^{i\omega t}\right] \quad (62)$$

$$\hat{u}_\theta(z, r, \theta, t) = J_n\left(\pi\beta_{m,n}\frac{r}{R}\right)\mathcal{R}e \left[\left(\eta_{\theta,f}fe^{-ik_{f,p}(z)} + \eta_{\theta,g}ge^{-ik_{g,p}(z)}\right)\left(Pe^{-in\theta} - Qe^{in\theta}\right)e^{i\omega t}\right] \quad (63)$$

$$\hat{u}_z(z, r, \theta, t) = J_n\left(\pi\beta_{m,n}\frac{r}{R}\right)\mathcal{R}e \left[\left(fe^{-ik_{f,u}(z)} - ge^{-ik_{g,u}(z)}\right)\left(Pe^{-in\theta} + Qe^{in\theta}\right)e^{i\omega t}\right] \quad (64)$$

The correction factors for the radial and tangential velocity can be obtained by substituting the pressure and velocity into the respective momentum equations, said factors are shown in equations (65) and (66), respectively. Note that the same equation applies to both the f and g correction factors of θ and r, but the initial conditions will be different. As previously stated, the correction factor for the axial velocity is absorbed into the exponents, consequently it can be represented as shown in equation (67), similarly to the 1D case.

$$\eta_r\left[\frac{i\omega}{c_0} + M_{z,0}\left(\frac{1}{\eta_r}\frac{\partial\eta_r}{\partial z} - i\frac{\partial k_p}{\partial z}\right)\right] = -1 \quad (65)$$

$$\eta_\theta\left[\frac{i\omega}{c_0} + M_{z,0}\left(\frac{1}{\eta_\theta}\frac{\partial\eta_\theta}{\partial z} - i\frac{\partial k_p}{\partial z}\right)\right] = i\frac{n}{r} \quad (66)$$

$$\eta_{z,f} = e^{-i(k_{f,u}-k_{f,p})}, \quad \eta_{z,g} = -e^{-i(k_{g,u}-k_{g,p})} \quad (67)$$

Note that, in equations (65) and (66), the derivation has been conducted considering the value R in the argument of the Bessel function to be constant. For a geometry of varying area, this would not be the case and several new terms would appear, as well as in the rest of equations that will be derived later on, for simplicity, this terms will be omitted and it will later be justified why it is chosen to do so. The example of the extra terms that would appear is shown in the following equation:

$$\frac{\partial(\hat{u}_\theta)}{\partial z} = -\hat{u}_\theta\left[i\frac{\partial k}{\partial z} + \frac{1}{J_n}\frac{\partial J_n}{\partial(r/R)}\frac{r}{R^2}\frac{\partial R}{\partial z}\right] \quad \text{insteadof} \quad \frac{\partial(\hat{u}_\theta)}{\partial z} = -i\hat{u}_\theta\frac{\partial k}{\partial z} \quad (68)$$

Substituting the acoustic pressure and axial velocity into the axial momentum equation and considering that the forward and backward axial waves need to independently solve the system, equations (69) and (70) are obtained.

$$\left(M_{z,0}^2 - 1\right)\frac{1}{u_{z,0}}\frac{\partial u_{z,0}}{\partial z} + \frac{1}{c_0}\frac{\partial c_0}{\partial z} - \frac{1}{A}\frac{\partial A}{\partial z} - i\frac{\partial k_{f,p}}{\partial z} = \left(-\frac{i\omega}{c_0} + iM_{z,0}\frac{\partial k_{f,u}}{\partial z} - M_{z,0}\frac{1}{u_{z,0}}\frac{\partial u_{z,0}}{\partial z}\right)\eta_{z,f} \quad (69)$$

$$\left(M_{z,0}^2 - 1\right)\frac{1}{u_{z,0}}\frac{\partial u_{z,0}}{\partial z} + \frac{1}{c_0}\frac{\partial c_0}{\partial z} - \frac{1}{A}\frac{\partial A}{\partial z} - i\frac{\partial k_{g,p}}{\partial z} = \left(-\frac{i\omega}{c_0} + iM_{z,0}\frac{\partial k_{g,u}}{\partial z} - M_{z,0}\frac{1}{u_{z,0}}\frac{\partial u_{z,0}}{\partial z}\right)\eta_{z,g} \quad (70)$$

Which can be re-arranged to express the derivative of the velocity exponent with respect to the pressure exponent and other variables, as shown in the following equation:

$$i\frac{\partial k_u}{\partial z} = \frac{\pm 1}{M_{z,0}}\left[\left(M_{z,0}^2 - 1\right)\frac{1}{u_{z,0}}\frac{\partial u_{z,0}}{\partial z} + \frac{1}{c_0}\frac{\partial c_0}{\partial z} - \frac{1}{A}\frac{\partial A}{\partial z} - i\frac{\partial k_p}{\partial z}\right] \times \frac{1}{\eta_z} + \frac{i\omega}{M_{z,0}c_0} + \frac{1}{u_{z,0}}\frac{\partial u_{z,0}}{\partial z} \quad (71)$$

Substituting all acoustic variables into the continuity equation, which also needs to be independently solved for the forward and backward waves, the following relation is obtained:

$$\frac{i\omega}{c_0} - \frac{M_{z,0}}{A}\frac{\partial A}{\partial z} - \frac{M_{z,0}}{c_0}\frac{\partial c_0}{\partial z} - iM_{z,0}\frac{\partial k_p}{\partial z} + \frac{\eta_r}{J_n}\frac{\partial^2 J_n}{\partial r^2} + \frac{\eta_r}{rJ_n}\frac{\partial J_n}{\partial r} - \frac{in}{r}\eta_\theta \mp \left(i\frac{\partial k_u}{\partial z} + \frac{1}{A}\frac{\partial A}{\partial z} + \frac{1}{u_{z,0}}\frac{\partial u_{z,0}}{\partial z}\right)\eta_z = 0 \quad (72)$$

In order to find a solution to this equation, a new variable χ will need to be introduced, which relates to the correction factors of the radial and tangential velocity as shown in equation (73). Note that χ also has different solutions for f and g, due to different initial conditions.

$$\chi = -\eta_r, \quad \eta_\theta = i\frac{n}{r}\chi \quad (73)$$

Substituting this variable into the continuity equation and performing some re-arrangement, equation (74) is obtained.

$$r^2\frac{\partial^2 J_n}{\partial r^2}+r\frac{\partial J_n}{\partial r}+\left[\frac{-1}{\chi}\left(\frac{i\omega}{c_0}-\frac{M_{z,0}}{A}\frac{\partial A}{\partial z}-\frac{M_{z,0}}{c_0}\frac{\partial c_0}{\partial z}-iM_{z,0}\frac{\partial k_p}{\partial z}\mp\left(i\frac{\partial k_u}{\partial z}+\frac{1}{A}\frac{\partial A}{\partial z}+\frac{1}{u_{z,0}}\frac{\partial u_{z,0}}{\partial z}\right)\eta_z\right)r^2-n^2\right]J_n=0 \tag{74}$$

If the reader is familiarized with Bessel equations, it will be easily recognized that equation (74) corresponds to the Bessel equation. Since J_n is the Bessel function of order n, it will satisfy the equation as long as equation (75) is satisfied.

$$\frac{\pi^2\beta_{m,n}^2}{R^2}=\frac{-1}{\chi}\left(\frac{i\omega}{c_0}-\frac{M_{z,0}}{A}\frac{\partial A}{\partial z}-\frac{M_{z,0}}{c_0}\frac{\partial c_0}{\partial z}-iM_{z,0}\frac{\partial k_p}{\partial z}\mp\left(i\frac{\partial k_u}{\partial z}+\frac{1}{A}\frac{\partial A}{\partial z}+\frac{1}{u_{z,0}}\frac{\partial u_{z,0}}{\partial z}\right)\eta_z\right) \tag{75}$$

At this point, it becomes clear why the terms that result of the radius of the geometry not being constant (a function of the axial variable) were disregarded. These terms contain the derivative of the Bessel function with respect to the radius, which would result in equation (74) no longer being the Bessel equation (contrary to the other terms function of the area variation that were kept in the derivation). Consequently, the Bessel function would no longer be a solution of it and the initial assumption of the acoustic pressure and velocities shapes would also not be valid. The final equation would be a partial differential equation of two variables (axial and radial) which would significantly increase the computational cost and was, therefore, not implemented. As the area variation cannot be described with the Bessel equation for the stated reasons, the terms function of the area variation that were kept up to this point should be removed.

For the 3D element with isentropic background flow but constant area section, the set of six equations that need to be solved are summarized next (equations (76) to (78)). The equations are shown only for the f wave as the results for g are identical for k_p, k_u, χ. The results for each wave are differentiated through initial conditions.

$$\begin{aligned}i\left(1-M_{z,0}^2\right)\frac{\partial k_{f,p}}{\partial z}=&-\frac{\pi^2\beta_{m,n}^2}{R^2}\chi_f M_{z,0}\\&+\left(M_{z,0}^2+2M_{z,0}\eta_{z,f}-1\right)\\&\quad\frac{1}{u_{z,0}}\frac{\partial u_{z,0}}{\partial z}+\left(M_{z,0}^2+1\right)\frac{1}{c_0}\frac{\partial c_0}{\partial z}\\&+\left(M_{z,0}(\eta_{z,f}+M_{z,0})-1\right)\frac{1}{A}\frac{\partial A}{\partial z}\\&+(\eta_{z,f}-M_{z,0})\frac{i\omega}{c_0}\end{aligned} \tag{76}$$

$$\begin{aligned}i\frac{\partial k_{f,u}}{\partial z}=&\frac{1}{M_{z,0}}\left[\left(M_{z,0}^2-1\right)\frac{1}{u_{z,0}}\frac{\partial u_{z,0}}{\partial z}+\frac{1}{c_0}\frac{\partial c_0}{\partial z}-\frac{1}{A}\frac{\partial A}{\partial z}-i\frac{\partial k_{f,p}}{\partial z}\right]\\&\times\frac{1}{\eta_{z,f}}+\frac{i\omega}{M_{z,0}c_0}+\frac{1}{u_{z,0}}\frac{\partial u_{z,0}}{\partial z}\end{aligned} \tag{77}$$

$$M_{z,0}\frac{\partial\chi_f}{\partial z}=1-\chi_f\left(\frac{i\omega}{c_0}-iM_{z,0}\frac{\partial k_{f,p}}{\partial z}\right) \tag{78}$$

Once more, the upstream boundary conditions for the wave numbers and correction factors are taken to match the results of the 3D incompressible tube. This way, if the terms for background flow gradients are removed, the solutions for the incompressible case are recovered. The initial conditions are as follows:

$$k_{f,p}(0)=k_{g,p}(0)=0 \tag{79}$$

$$\frac{\partial k_{f,p}}{\partial z}(0)=\frac{\omega/c_0}{1-M_{z,0}^2}\left(\sqrt{1-\left(\frac{\pi\beta_{m,n}}{R}\right)^2\left(\frac{c_0}{\omega}\right)^2\left(1-M_{z,0}^2\right)}-M_{z,0}\right) \tag{80}$$

$$\frac{\partial k_{g,p}}{\partial z}(0)=\frac{-\omega/c_0}{1-M_{z,0}^2}\left(\sqrt{1-\left(\frac{\pi\beta_{m,n}}{R}\right)^2\left(\frac{c_0}{\omega}\right)^2\left(1-M_{z,0}^2\right)}+M_{z,0}\right) \tag{81}$$

$$\chi_f(0)=\frac{-i}{\omega/c_0-M_{z,0}\frac{\partial k_{f,p}}{\partial z}(0)} \tag{82}$$

$$\chi_g(0)=\frac{-i}{\omega/c_0-M_{z,0}\frac{\partial k_{g,p}}{\partial z}(0)} \tag{83}$$

$$k_{f,u}(0)=\ln\left[i\chi_f(0)\frac{\partial k_{f,p}}{\partial z}(0)\right]+k_{f,p}(0) \tag{84}$$

$$k_{g,u}(0)=\ln\left[-i\chi_g(0)\frac{\partial k_{g,p}}{\partial z}(0)\right]+k_{g,p}(0) \tag{85}$$

Full derivation of novel sonic BC. This new model employs the continuity and momentum equations in their acoustic form, following the assumptions from the 1D isentropic case (equations (38) and (39)). At the throat of a rocket engine nozzle (convergent to divergent transition), the derivative of the area is zero, allowing to remove said terms from the equations. Moreover, for a purely axial background flow, the background flow Mach number is unity at the throat. The resulting expressions are as follows:

$$\left(i\omega + \frac{\partial c_0}{\partial x} - ic_0 \frac{\partial k_p}{\partial x}\right)\frac{\hat{p}}{\rho_0 c_0} + \left(-\frac{\partial u_0}{\partial x} - ic_0 \frac{\partial k_u}{\partial x}\right)\hat{u} = 0 \tag{86}$$

$$\left(\frac{\partial c_0}{\partial x} - ic_0 \frac{\partial k_p}{\partial x}\right)\frac{\hat{p}}{\rho_0 c_0} + \left(i\omega - ic_0 \frac{\partial k_u}{\partial x} + \frac{\partial u_0}{\partial x}\right)\hat{u} = 0 \tag{87}$$

If the difference of both equations is taken, all the terms containing k_p and k_u disappear, resulting in an expression function only of the acoustic pressure and velocity (requirement for a BC):

$$i\omega \frac{\hat{p}}{\rho_0 c_0} - \left(i\omega + 2\frac{\partial u_0}{\partial x}\right)\hat{u} = 0 \tag{88}$$

As the BC was derived from the same equations as the acoustic model that describes the evolution of f and g, one might think that this BC offers no new information, as it should already be satisfied through the acoustic calculations. Nevertheless, in the equations of the acoustic models, such as equation (44), the derivative of the wave number cannot be computed at the throat, as the term $(1 - M_0^2)$ is dividing, which results in an infinite derivative of k_p at the throat. Consequently, the acoustic model should not be employed near the throat in that shape. On the other hand, the BC avoids this issue altogether and can be applied at the throat without any issue. As a result, the set of solutions of the acoustic model which also comply with this new sonic BC will correspond to the acoustic resonant frequencies of the system.

The sonic BC for an acoustic 3D non-isentropic flow is shown in equation (10), which has been derived in the same fashion from equation (sec). Note that the heat release at the throat has been disregarded. To obtain the 3D isentropic BC, it is sufficient to substitute $\hat{\rho} = \frac{\hat{p}}{c_0^2}$ in the non-isentropic expression.

Full derivation of 1D distributed flame model with area variation. The employed hypothesis are no viscosity or losses, no body forces and no heat transfer to the walls. Moreover, the flow is treated as 1D and a heat addition due to chemical reactions is considered throughout the flame length. Consequently, neither the background flow nor the acoustics can be considered isentropic throughout the span of the flame. The heat release of the background flow is assumed to be known, but the distributed flame model requires an unsteady heat release model. The resulting continuity, momentum and energy equations are as follows:

$$\frac{\partial(\rho A)}{\partial t} + \frac{\partial(\rho u A)}{\partial x} = 0 \tag{89}$$

$$\rho \frac{\partial u}{\partial t} + \rho u \frac{\partial u}{\partial x} + \frac{\partial p}{\partial x} = 0 \tag{90}$$

$$\rho T \frac{DS}{Dt} = Q \tag{91}$$

where a capital D represents the substantial derivative and Q represents the addition of heat due to chemical reactions (per unit time and unit volume). Applying the entropy differential (equation (92)), the energy equation can be written in terms of density and pressure as shown in equation (93). Then, employing the speed of sound definition and assuming that the fluid is a perfect gas, the expression can be further simplified to equation (94).

$$dS = \left(\frac{\partial S}{\partial p}\right)_\rho dp + \left(\frac{\partial S}{\partial \rho}\right)_p d\rho \tag{92}$$

$$\frac{\partial p}{\partial t} + u\frac{\partial p}{\partial x} + \frac{\left(\frac{\partial S}{\partial \rho}\right)_p}{\left(\frac{\partial S}{\partial p}\right)_\rho}\left(\frac{\partial \rho}{\partial t} + u\frac{\partial \rho}{\partial x}\right) = \frac{Q}{\rho T}\frac{1}{\left(\frac{\partial S}{\partial p}\right)_\rho} \tag{93}$$

$$\frac{\partial p}{\partial t} + u\frac{\partial p}{\partial x} - c^2\left(\frac{\partial \rho}{\partial t} + u\frac{\partial \rho}{\partial x}\right) = (\gamma - 1)Q \tag{94}$$

In order to model the acoustics, it will be considered that pressure, density, velocity, temperature and speed of sound have a ‘background flow’ component and an ‘acoustics’ component, where the acoustic component is small in comparison with the background flow value. Consequently, these variables can be expressed as shown in equation (95). Furthermore, all background variables are purely a function of the longitudinal variable, explicitly written in equation (96). Note that, γ has been considered to not have an acoustic component, this is done to reduce the complexity of the model, since the chemical reactions generated by the acoustics are not sufficient to generate a significant change in the value of γ. On the other hand, the background flow chemical reactions might change γ significantly, so its value can be a function of the axial coordinate.

$$\begin{aligned} p &= p_0 + \hat{p}(t,x), \quad \rho = \rho_0 + \hat{\rho}(t,x), \\ u &= u_0 + \hat{u}(t,x), \quad c = c_0 + \hat{c}(t,x), \\ T &= T_0 + \hat{T}(t,x) \end{aligned} \tag{95}$$

$$\begin{aligned} &u_0 \equiv u_o(x), \quad p_0 \equiv p_0(x), \quad \rho_0 \equiv \rho_0(x), \\ &c_0 \equiv c_0(x), \quad T_0 \equiv T_0(x), \quad A \equiv A(x), \quad \gamma \equiv \gamma(x) \end{aligned} \tag{96}$$

The acoustic component of the temperature equation can be easily expressed in terms of the acoustic pressure and density through the equation of state, as shown in equation (97). Furthermore, the acoustic speed of sound can also be expressed in terms of the acoustic pressure and density through its definition if the perfect gas relations are applied, as shown in equation (98).

$$\hat{T} = T_0\left(\frac{\hat{p}}{p_0} - \frac{\hat{\rho}}{\rho_0}\right) \tag{97}$$

$$\frac{\hat{c}}{c_0} = \frac{1}{2}\frac{\hat{T}}{T_0} = \frac{1}{2}\left(\frac{\hat{p}}{p_0} - \frac{\hat{\rho}}{\rho_0}\right) \tag{98}$$

Equations (95) and (96) are substituted into equations (89), (90) and (94). Considering that the background flow already satisfies the equations and that the acoustics are linearized (products of two or more acoustic variables are removed from the equations), the resulting expressions are shown subsequently:

$$\begin{aligned} &A\frac{\partial\hat{\rho}}{\partial t} + u_0 A\frac{\partial\hat{\rho}}{\partial x} + A\hat{\rho}\frac{\partial u_0}{\partial x} + u_0\hat{\rho}\frac{\partial A}{\partial x} \\ &+ \dot{m}\left(\frac{1}{u_0}\frac{\partial\hat{u}}{\partial x} - \frac{\hat{u}}{u_0^2}\frac{\partial u_0}{\partial x}\right) \\ &= 0 \end{aligned} \tag{99}$$

$$\rho_0\frac{\partial\hat{u}}{\partial t} + \rho_0 u_0\frac{\partial\hat{u}}{\partial x} + \rho_0\hat{u}\frac{\partial u_0}{\partial x} + \hat{\rho}u_0\frac{\partial u_0}{\partial x} + \frac{\partial\hat{p}}{\partial x} = 0 \tag{100}$$

$$\begin{aligned} &\frac{\partial\hat{p}}{\partial t} + u_0\frac{\partial\hat{p}}{\partial x} + \hat{u}\frac{\partial p_0}{\partial x} - c_0^2\left(\frac{\partial\hat{\rho}}{\partial t} + u_0\frac{\partial\hat{\rho}}{\partial x} + \hat{u}\frac{\partial\rho_0}{\partial x}\right) \\ &- 2c_0u_0\frac{\partial\rho_0}{\partial x}\hat{c} = (\gamma - 1)\hat{\dot{Q}} \end{aligned} \tag{101}$$

Following a similar approach to the isentropic elements, the energy equation will be analysed first, in order to achieve a correlation between the acoustic density and acoustic pressure. For an isentropic background flow: $\hat{\rho} = \hat{p}/c_0^2$, consequently, it will be assumed that, for the novel more generic case, the shape is given by equation (104). The shape of the acoustic pressure and acoustic velocity will be assumed to be the same as the one used in the derivations for the isentropic elements, as shown in equations (102) and (103).

$$\begin{aligned} \hat{p} &= \rho_0c_0(f_p + g_p)e^{i\omega t} \\ &= \rho_0c_0\mathcal{R}e\left[\left(f_0e^{-ik_{f,p}(x)} + g_0e^{-ik_{g,p}(x)}\right)e^{i\omega t}\right] \end{aligned} \tag{102}$$

$$\begin{aligned} \hat{u} &= (f_u + g_u)e^{i\omega t} = \left(\eta_{u,f}f_p + \eta_{u,g}g_p\right)e^{i\omega t} \\ &= \mathcal{R}e\left[\left(f_0e^{-ik_{f,u}(x)} - g_0e^{-ik_{g,u}(x)}\right)e^{i\omega t}\right] \end{aligned} \tag{103}$$

$$\begin{aligned} \hat{\rho} &= \frac{\rho_0}{c_0}(f_\rho + g_\rho)e^{i\omega t} = \frac{\rho_0}{c_0}\left(\eta_{\rho,f}f_p + \eta_{\rho,g}g_p\right)e^{i\omega t} \\ &= \frac{\rho_0}{c_0}\mathcal{R}e\left[\left(f_0e^{-ik_{f,\rho}(x)} + g_0e^{-ik_{g,\rho}(x)}\right)e^{i\omega t}\right] \end{aligned} \tag{104}$$

$$\begin{aligned} &\eta_{f,u} = e^{-i(k_{f,u} - k_{f,p})}, \quad \eta_{g,u} = -e^{-i(k_{g,u} - k_{g,p})}, \\ &\eta_{f,\rho} = e^{-i(k_{f,\rho} - k_{f,p})}, \quad \eta_{g,\rho} = e^{-i(k_{g,\rho} - k_{g,p})} \end{aligned} \tag{105}$$

Substituting these expressions into the continuity, momentum and energy equations, allows to evaluate the various derivatives. This results in equations (106) to (108), respectively.

$$\left[\frac{i\omega}{c_0} - \frac{M_0}{c_0}\frac{\partial c_0}{\partial x} - iM_0\frac{\partial k_\rho}{\partial x}\right]\frac{\hat{\rho}}{\rho_0/c_0} + \left[-i\frac{\partial k_u}{\partial x} - \frac{1}{u_0}\frac{\partial u_0}{\partial x}\right]\hat{u} = 0 \tag{106}$$

$$\begin{aligned} &\left[\frac{M_0^2}{u_0}\frac{\partial u_0}{\partial x}\right]\frac{\hat{\rho}}{\rho_0/c_0} + \left[\frac{i\omega}{c_0} - iM_0\frac{\partial k_u}{\partial x} + \frac{M_0}{u_0}\frac{\partial u_0}{\partial x}\right]\hat{u} \\ &+ \left[\frac{1}{\rho_0}\frac{\partial\rho_0}{\partial x} + \frac{1}{c_0}\frac{\partial c_0}{\partial x} - i\frac{\partial k_p}{\partial x}\right]\frac{\hat{p}}{\rho_0c_0} \\ &= 0 \end{aligned} \tag{107}$$

$$\begin{aligned} &\left[i\omega + u_0\left(\frac{(1-\gamma)}{\rho_0}\frac{\partial\rho_0}{\partial x} + \frac{1}{c_0}\frac{\partial c_0}{\partial x} - i\frac{\partial k_p}{\partial x}\right)\right]\frac{\hat{p}}{\rho_0c_0} \\ &- \left[i\omega + u_0\left(-\frac{1}{c_0}\frac{\partial c_0}{\partial x} - i\frac{\partial k_\rho}{\partial x}\right)\right]\frac{\hat{\rho}}{\rho_0/c_0} + \\ &+ \left[\frac{\partial p_0}{\partial x} - c_0^2\frac{\partial\rho_0}{\partial x}\right]\frac{\hat{u}}{\rho c} = (\gamma - 1)n\frac{Q_0}{p_0}e^{-i\omega\tau}\frac{\hat{p}}{\rho_0c_0} \end{aligned} \tag{108}$$

In the energy equation, the expression for the acoustic speed of sound (equation (98)) as well as Crocco's simple time lag model based on acoustic pressure for the unsteady heat release (equation (109)) have also been substituted. A different expression for the unsteady heat release could also be used. As long as the unsteady heat release is a linear function of the acoustic variables, the rest of the derivation would be valid for any other description.

$$\begin{aligned} \frac{\hat{\dot{Q}}(t,x)}{\dot{Q}_0(x)} &= n(\omega,x)\frac{\hat{p}(t-\tau(\omega,x),x)}{p(x)} \\ &= n(\omega,x)\cdot e^{-i\tau(\omega,x)\omega}\frac{\hat{p}(t,x)}{p(x)} \end{aligned} \tag{109}$$

Next, the values of the acoustic pressure, density and velocity will be substituted into the equations. The equations need to be satisfied both for the f and g waves. This yields a total of six equations, in which the unknown variables corresponds to $k_{f,p}$, $k_{g,p}$, $k_{f,u}$, $k_{g,u}$, $k_{f,\rho}$ and $k_{g,\rho}$. The continuity equation has been substituted into the energy equations and all the equations have been re-arranged in order to present the final system of equations to be solved:

$$\begin{aligned} -i\frac{\partial k_\rho}{\partial x}\eta_\rho &= \left[-\frac{i\omega}{c_0}\frac{1}{M_0} + \frac{1}{c_0}\frac{\partial c_0}{\partial x}\right]\eta_\rho \\ &+ \frac{1}{M_0}\left[i\frac{\partial k_u}{\partial x} + \frac{1}{u_0}\frac{\partial u_0}{\partial x}\right]\eta_u \end{aligned} \tag{110}$$

$$\begin{aligned} i\frac{\partial k_u}{\partial x} &= \left[\frac{M_0}{u_0}\frac{\partial u_0}{\partial x}\right]\frac{\eta_\rho}{\eta_u} + \left[\frac{i\omega}{c_0}\frac{1}{M_0} + \frac{1}{u_0}\frac{\partial u_0}{\partial x}\right] \\ &+ \left[-\frac{i}{M_0}\frac{\partial k_p}{\partial x} + \frac{1}{M_0\rho_0}\frac{\partial\rho_0}{\partial x} + \frac{1}{M_0c_0}\frac{\partial c_0}{\partial x}\right]\frac{1}{\eta_u} \end{aligned} \tag{111}$$

$$- i\left(1 - M_0^2\right)\frac{\partial k_p}{\partial x} = \left[-\frac{i\omega}{c_0} - \frac{1-\gamma}{\gamma}\frac{M_0}{A}\frac{\partial A}{\partial x} - \frac{\gamma+1}{\gamma}\frac{M_0}{u_0}\frac{\partial u_0}{\partial x} + \frac{2}{\gamma}\frac{M_0}{c_0}\frac{\partial c_0}{\partial x}\right]\eta_u - \left[\frac{M_0^2}{u_0}\frac{\partial u_0}{\partial x}\right]\eta_\rho + \left[\frac{i\omega}{c_0}M_0 + \left(\left(1-\gamma\right)M_0^2 - 1\right)\frac{1}{\rho_0}\frac{\partial \rho_0}{\partial x} + \left(M_0^2 - 1\right)\frac{1}{c_0}\frac{\partial c_0}{\partial x} - M_0\left(\gamma - 1\right)n_{flame}\frac{\gamma Q_0}{\rho_0 c_0^3}e^{-i\omega\tau}\right] \tag{112}$$

Once again, the equations look the same for the f and g waves, the difference residing in the initial conditions:

$$k_{f,p}(0) = 0, \quad k_{g,p}(0) = 0, \quad k_{f,u}(0) = 0, \quad k_{g,u}(0) = 0, \quad k_{f,\rho}(0) = 0, \quad k_{g,\rho}(0) = 0 \tag{113}$$

$$\eta_{f,p}(0) = 1, \quad \eta_{g,p}(0) = 1, \quad \eta_{f,\rho}(0) = 1, \quad \eta_{g,\rho}(0) = 1, \quad \eta_{f,u}(0) = 1, \quad \eta_{g,u}(0) = -1 \tag{114}$$

Full derivation of 3D distributed flame model. The hypothesis are identical to the 1D case. In 3D, the resulting equations of continuity, momentum and energy are as follows:

$$\frac{\partial \rho}{\partial t} + \frac{1}{r}\left(\frac{\partial\left(\rho r u_r\right)}{\partial r} + \frac{\partial\left(\rho u_\theta\right)}{\partial \theta} + \frac{\partial\left(\rho r u_z\right)}{\partial z}\right) = 0 \tag{115}$$

$$\rho\left(\frac{\partial u_r}{\partial t} + u_r\frac{\partial u_r}{\partial r} + \frac{u_\theta}{r}\frac{\partial u_r}{\partial \theta} + u_z\frac{\partial u_r}{\partial z} - \frac{u_\theta^2}{r}\right) = -\frac{\partial p}{\partial r} \tag{116}$$

$$\rho\left(\frac{\partial u_\theta}{\partial t} + u_r\frac{\partial u_\theta}{\partial r} + \frac{u_\theta}{r}\frac{\partial u_\theta}{\partial \theta} + u_z\frac{\partial u_\theta}{\partial z} - \frac{u_\theta u_r}{r}\right) = -\frac{1}{r}\frac{\partial p}{\partial \theta} \tag{117}$$

$$\rho\left(\frac{\partial u_z}{\partial t} + u_r\frac{\partial u_z}{\partial r} + \frac{u_\theta}{r}\frac{\partial u_z}{\partial \theta} + u_z\frac{\partial u_z}{\partial z}\right) = -\frac{\partial p}{\partial z} \tag{118}$$

$$\frac{\partial S}{\partial t} + u_r\frac{\partial S}{\partial r} + \frac{u_\theta}{r}\frac{\partial S}{\partial \theta} + u_z\frac{\partial S}{\partial z} = \frac{Q}{\rho T} \tag{119}$$

Similarly to the 1D case, employing the entropy differential shown in equation (92), the energy equation can be re-written in terms of the density and pressure, assuming that the fluid behaves as a perfect gas. The resulting expression is as follows:

$$\frac{\partial p}{\partial t} + u_r\frac{\partial p}{\partial r} + \frac{u_\theta}{r}\frac{\partial p}{\partial \theta} + u_z\frac{\partial p}{\partial z} - c^2\left(\frac{\partial \rho}{\partial t} + u_r\frac{\partial \rho}{\partial r} + \frac{u_\theta}{r}\frac{\partial \rho}{\partial \theta} + u_z\frac{\partial \rho}{\partial z}\right) = \left(\gamma - 1\right)Q \tag{120}$$

Once more, all the variables will be substituted by the sum of their background flow component and their acoustic component, as shown in equation (121). Note that the background flow is considered 1D even if the acoustics are 3D, so the tangential and radial velocities are zero, as stated in equation (122). The area is considered constant, as it was seen that implementing a variable area into the 3D formulation is not feasible with the current approach.

$$p = p_0 + \hat{p}(t, r, \theta, z), \quad \rho = \rho_0 + \hat{\rho}(t, r, \theta, z), \quad u = u_0 + \hat{u}(t, r, \theta, z), \quad c = c_0 + \hat{c}(t, r, \theta, z) \tag{121}$$

$$u_{r,0} = 0, \quad u_{\theta,0} = 0, \quad u_{z,0} \equiv u_{z,0}(z), \quad p_0 \equiv p_0(z), \quad \rho_0 \equiv \rho_0(z), \quad c \equiv c(z), \quad \gamma \equiv \gamma(z) \tag{122}$$

As in the 1D case, the energy equation will be analysed first in order to achieve a correlation between the acoustic density and the acoustic pressure. Substituting all variables for their background flow and acoustic components and linearizing, the energy equation can be written as follows:

$$\frac{\partial \hat{p}}{\partial t} + u_{z,0}\frac{\partial \hat{p}}{\partial z} + \hat{u}_z\frac{\partial p_0}{\partial z} - c_0^2\left(\frac{\partial \hat{\rho}}{\partial t} + u_{z,0}\frac{\partial \hat{\rho}}{\partial z} + \hat{u}_z\frac{\partial \rho_0}{\partial z}\right) - 2c_0u_{z,0}\frac{\partial \rho_0}{\partial z}\hat{c} = \left(\gamma - 1\right)\hat{Q} \tag{123}$$

All the terms related to the tangential and radial spatial dimensions have been eliminated through linearization. Consequently, the same resulting expression for the energy equation used in the 1D case can also be employed in the 3D case, presented in the following equation:

$$\left[i\omega + u_0\left(\frac{(1-\gamma)}{\rho_0}\frac{\partial \rho_0}{\partial x} + \frac{1}{c_0}\frac{\partial c_0}{\partial x} - i\frac{\partial k_p}{\partial x}\right)\right]\frac{\hat{p}}{\rho_0 c_0} - \left[i\omega + u_0\left(-\frac{1}{c_0}\frac{\partial c_0}{\partial x} - i\frac{\partial k_\rho}{\partial x}\right)\right]\frac{\hat{\rho}}{\rho_0/c_0} + \left[\frac{\partial p_0}{\partial x} - c_0^2\frac{\partial \rho_0}{\partial x}\right]\frac{\hat{u}}{\rho c} = \left(\gamma - 1\right)n\frac{Q_0}{p_0}e^{-i\omega\tau}\frac{\hat{p}}{\rho_0 c_0} \tag{124}$$

Substituting equations (121) into (115) and into (116) to (118), the following relations are obtained:

$$\frac{\partial \hat{\rho}}{\partial t} + \frac{1}{r}\left(\frac{\partial\left(\rho_0 r\hat{u}_r\right)}{\partial r} + \frac{\partial\left(\rho_0\hat{u}_\theta\right)}{\partial \theta} + \frac{\partial\left(\rho_0 r\hat{u}_z\right)}{\partial z} + \frac{\partial\left(\hat{\rho} r u_{z,0}\right)}{\partial z}\right) = 0 \tag{125}$$

$$\rho_0\left(\frac{\partial \hat{u}_r}{\partial t} + u_{z,0}\frac{\partial \hat{u}_r}{\partial z}\right) = -\frac{\partial \hat{p}}{\partial r} \tag{126}$$

$$\rho_0\left(\frac{\partial \hat{u}_\theta}{\partial t} + u_{z,0}\frac{\partial \hat{u}_\theta}{\partial z}\right) = -\frac{1}{r}\frac{\partial \hat{p}}{\partial \theta} \tag{127}$$

$$\rho_0\left(\frac{\partial \hat{u}_z}{\partial t}+u_{z,0}\frac{\partial \hat{u}_z}{\partial z}+\hat{u}_z\frac{\partial u_{z,0}}{\partial z}\right)+\hat{\rho}u_{z,0}\frac{\partial u_{z,0}}{\partial z}=-\frac{\partial \hat{p}}{\partial z} \quad (128)$$

The shape of the acoustic variables in the 3D case are as follows:

$$\hat{p}(t,r,\theta,z)=\rho_0 c_0 J_n\left(\pi\beta_{m,n}\frac{r}{R}\right)\mathcal{R}e\left[\left(fe^{-ik_{f,p}(z)}+ge^{-ik_{g,p}(z)}\right)\left(Pe^{-in\theta}+Qe^{in\theta}\right)e^{i\omega t}\right] \quad (129)$$

$$\hat{u}_r(t,r,\theta,z)=\frac{\partial J_n\left(\pi\beta_{m,n}\frac{r}{R}\right)}{\partial r}\mathcal{R}e\left[\left(\eta_{r,f}fe^{-ik_{f,p}(z)}+\eta_{r,g}ge^{-ik_{g,p}(z)}\right)\left(Pe^{-in\theta}+Qe^{in\theta}\right)e^{i\omega t}\right] \quad (130)$$

$$\hat{u}_\theta(t,r,\theta,z)=J_n\left(\pi\beta_{m,n}\frac{r}{R}\right)\mathcal{R}e\left[\left(\eta_{\theta,f}fe^{-ik_{f,p}(z)}+\eta_{\theta,g}ge^{-ik_{g,p}(z)}\right)\left(Pe^{-in\theta}-Qe^{in\theta}\right)e^{i\omega t}\right] \quad (131)$$

$$\hat{u}_z(t,r,\theta,z)=J_n\left(\pi\beta_{m,n}\frac{r}{R}\right)\mathcal{R}e\left[\left(fe^{-ik_{f,u}(z)}-ge^{-ik_{g,u}(z)}\right)\left(Pe^{-in\theta}+Qe^{in\theta}\right)e^{i\omega t}\right] \quad (132)$$

$$\hat{\rho}(t,r,\theta,z)=\frac{\rho_0}{c_0}J_n\left(\pi\beta_{m,n}\frac{r}{R}\right)\mathcal{R}e\left[\left(\eta_{\rho,f}fe^{-ik_{f,p}(z)}+\eta_{\rho,g}ge^{-ik_{g,p}(z)}\right)\left(Pe^{-in\theta}+Qe^{in\theta}\right)e^{i\omega t}\right] \quad (133)$$

$$\eta_{z,f}=e^{-i(k_{f,u}-k_{f,p})},\quad \eta_{z,g}=e^{-i(k_{g,u}-k_{g,p})},\quad \eta_{\rho,f}=e^{-i(k_{f,\rho}-k_{f,p})},\quad \eta_{\rho,g}=e^{-i(k_{g,\rho}-k_{g,p})} \quad (134)$$

where the same shape as in the isentropic case has been used, with the addition of the acoustic density. Employing the expressions from equations (129) to (134) in the continuity and momentum equations all the derivatives can be evaluated, the following four expressions are obtained as a result:

$$\frac{c_0}{\rho_0}\left[\frac{i\omega}{c_0}+M_{z,0}\left(\frac{1}{\rho_0}\frac{\partial \rho_0}{\partial z}-\frac{1}{c_0}\frac{\partial c_0}{\partial z}-i\frac{\partial k_\rho}{\partial z}\right)+M_{z,0}\frac{1}{u_{z,0}}\frac{\partial u_{z,0}}{\partial z}\right]\hat{\rho}+\left[\frac{1}{\partial J_n/\partial r}\frac{\partial^2 J_n}{\partial r^2}+\frac{1}{r}\right]\hat{u}_r+\left[\frac{\mp in}{r}\right]\hat{u}_\theta+\left[-i\frac{\partial k_u}{\partial z}+\frac{1}{\rho_0}\frac{\partial \rho_0}{\partial z}\right]\hat{u}_z=0 \quad (135)$$

$$\left(\frac{i\omega}{c_0}-iM_{z,0}\frac{\partial k_p}{\partial z}+M_{z,0}\frac{1}{\eta_r}\frac{\partial \eta_r}{\partial z}\right)\hat{u}_r=-\frac{\partial\left(\hat{p}/(\rho_0 c_0)\right)}{\partial r} \quad (136)$$

$$\left(\frac{i\omega}{c_0}-iM_{z,0}\frac{\partial k_p}{\partial z}+M_{z,0}\frac{1}{\eta_\theta}\frac{\partial \eta_\theta}{\partial z}\right)\hat{u}_\theta=-\frac{1}{r}\frac{\partial\left(\hat{p}/(\rho_0 c_0)\right)}{\partial \theta} \quad (137)$$

$$\left[\frac{i\omega}{c_0}-iM_{z,0}\frac{\partial k_u}{\partial z}+M_{z,0}\frac{1}{u_{z,0}}\frac{\partial u_{z,0}}{\partial z}\right]\hat{u}_z=\left[-M_{z,0}^2\frac{1}{u_{z,0}}\frac{\partial u_{z,0}}{\partial z}\right]\frac{\hat{\rho}}{\rho_0/c_0}-\left[\frac{1}{\rho_0}\frac{\partial \rho_0}{\partial x}+\frac{1}{c_0}\frac{\partial c_0}{\partial x}-i\frac{\partial k_p}{\partial z}\right]\frac{\hat{p}}{\rho_0 c_0} \quad (138)$$

Next, all acoustic variables can be written in terms of the acoustic pressure using the conversion factors η. Consequently, the acoustic pressure can be removed from all five equations and the resulting expressions are as follows:

$$\left[\frac{i\omega}{c_0}+M_{z,0}\left(\frac{1}{\rho_0}\frac{\partial \rho_0}{\partial z}-\frac{1}{c_0}\frac{\partial c_0}{\partial z}-i\frac{\partial k_\rho}{\partial z}\right)+M_{z,0}\frac{1}{u_{z,0}}\frac{\partial u_{z,0}}{\partial z}\right]\eta_\rho+\left[\frac{\partial^2 J_n}{\partial r^2}+\frac{1}{r}\frac{\partial J_n}{\partial r}\right]\frac{\eta_r}{J_n}+\left[\frac{-in}{r}\right]\eta_\theta+\left[-i\frac{\partial k_u}{\partial z}+\frac{1}{\rho_0}\frac{\partial \rho_0}{\partial z}\right]\eta_z=0 \quad (139)$$

$$\eta_r\left[\frac{i\omega}{c}+M_{z,0}\left(\frac{1}{\eta_r}\frac{\partial \eta_r}{\partial z}-i\frac{\partial k_p}{\partial z}\right)\right]=-1 \quad (140)$$

$$\eta_\theta\left[\frac{i\omega}{c}+M_{z,0}\left(\frac{1}{\eta_\theta}\frac{\partial \eta_\theta}{\partial z}-i\frac{\partial k_p}{\partial z}\right)\right]=i\frac{n}{r} \quad (141)$$

$$\left[\frac{i\omega}{c_0}-iM_{z,0}\frac{\partial k_u}{\partial z}+M_{z,0}\frac{1}{u_{z,0}}\frac{\partial u_{z,0}}{\partial z}\right]\eta_z=\left[-M_{z,0}^2\frac{1}{u_{z,0}}\frac{\partial u_{z,0}}{\partial z}\right]\eta_\rho-\left[\frac{1}{\rho_0}\frac{\partial \rho_0}{\partial z}+\frac{1}{c_0}\frac{\partial c_0}{\partial z}-i\frac{\partial k_p}{\partial z}\right] \quad (142)$$

$$\left[\frac{i\omega}{c_0}+M_{z,0}\left(\frac{(1-\gamma)}{\rho_0}\frac{\partial \rho_0}{\partial z}+\frac{1}{c_0}\frac{\partial c_0}{\partial z}-i\frac{\partial k_p}{\partial z}\right)\right]-\left[\frac{i\omega}{c_0}+M_{z,0}\left(-\frac{1}{c_0}\frac{\partial c_0}{\partial z}-i\frac{\partial k_\rho}{\partial z}\right)\right]\eta_\rho+\left[\frac{(1-\gamma)}{\gamma}\frac{1}{\rho_0}\frac{\partial \rho_0}{\partial z}-\frac{2}{\gamma}\frac{1}{c_0}\frac{\partial c_0}{\partial z}\right]\eta_z=\gamma(\gamma-1)n\frac{Q_0}{\rho_0 c_0^3}e^{-i\omega\tau} \quad (143)$$

Similarly to the 1D case, Crocco's simple time lag model (equation (109)) has been used in this derivation, but any other unsteady heat release model linearly dependent on the acoustic variables could be used in its place and the derivation would be valid. As was done in the isentropic case, an auxiliary variable will be introduced, which is related to the radial and tangential velocity correction factors as shown:

$$\chi=-\eta_r,\quad \eta_\theta=i\frac{n}{r}\chi \quad (144)$$

This auxiliary variable will then be substituted into the continuity equation, which will be multiplied by $\frac{r^2 J_n}{\chi}$ and reorganized to yield the following equation:

$$r^2\frac{\partial^2 J_n}{\partial r^2}+r\frac{\partial J_n}{\partial r}+\left[\left[\left(-\frac{i\omega}{c_0}+M_{z,0}\left(\frac{1}{c_0}\frac{\partial c_0}{\partial z}+i\frac{\partial k_\rho}{\partial z}\right)\right)\eta_\rho \pm\left(i\frac{\partial k_u}{\partial z}+\frac{1}{u_0}\frac{\partial u_0}{\partial z}\right)\eta_z\right]\frac{r^2}{\chi}-n^2\right]J_n=0 \quad (145)$$

This equation corresponds to the Bessel equation of order n, as it did in the isentropic case. Consequently, this equation relates the variables k_ρ, k_u. Along with the axial momentum and energy equations, all the variables of interest can be determined. Reorganizing the equations, the final system to be solved corresponds to:

$$-i\frac{\partial k_\rho}{\partial x}\eta_\rho=\left[-\frac{i\omega}{c_0}\frac{1}{M_0}+\frac{1}{c_0}\frac{\partial c_0}{\partial x}\right]\eta_\rho+\frac{1}{M_0}\left[i\frac{\partial k_u}{\partial x}+\frac{1}{u_0}\frac{\partial u_0}{\partial x}\right]\eta_u-\frac{\pi^2\beta_{m,n}^2}{R^2}\chi \quad (146)$$

$$i\frac{\partial k_u}{\partial x}=\left[\frac{M_0}{u_0}\frac{\partial u_0}{\partial x}\right]\frac{\eta_\rho}{\eta_u}+\left[\frac{i\omega}{c_0}\frac{1}{M_0}+\frac{1}{u_0}\frac{\partial u_0}{\partial x}\right]+\left[-\frac{i}{M_0}\frac{\partial k_p}{\partial x}-\frac{1}{M_0u_0}\frac{\partial u_0}{\partial x}+\frac{1}{M_0c_0}\frac{\partial c_0}{\partial x}\right]\frac{1}{\eta_u} \quad (147)$$

$$-i\left(1-M_0^2\right)\frac{\partial k_p}{\partial x}=\left[-\frac{i\omega}{c_0}-\frac{\gamma+1}{\gamma}\frac{M_0}{u_0}\frac{\partial u_0}{\partial x}+\frac{2}{\gamma}\frac{M_0}{c_0}\frac{\partial c_0}{\partial x}\right]\eta_u-\left[\frac{M_0^2}{u_0}\frac{\partial u_0}{\partial x}\right]\eta_\rho+\left[\frac{i\omega}{c_0}M_0-\left(\left(1-\gamma\right)M_0^2-1\right)\frac{1}{u_0}\frac{\partial u_0}{\partial x}+\left(M_0^2-1\right)\frac{1}{c_0}\frac{\partial c_0}{\partial x}-M_{z,0}\left(\gamma-1\right)n_{flame}\frac{\gamma Q_0}{\rho_0c_0^3}e^{-i\omega\tau}\right]+\frac{\pi^2\beta_{m,n}^2}{R^2}M_{z,0}\chi \quad (148)$$

$$M_{z,0}\frac{\partial\chi}{\partial z}=1-\chi\left(\frac{i\omega}{c}-iM_{z,0}\frac{\partial k_p}{\partial z}\right) \quad (149)$$

where the equations for f and g are identical, with them being differentiated by the upstream boundary conditions:

$$k_{f,p}(0)=k_{g,p}(0)=0,\quad k_{f,\rho}(0)=k_{g,\rho}(0)=0 \quad (150)$$

$$\frac{\partial k_{f,p}}{\partial z}(0)=\frac{\omega/c}{1-M_{z,0}^2}\left(\sqrt{1-\left(\frac{\pi\beta_{m,n}}{R}\right)^2\left(\frac{c}{\omega}\right)^2\left(1-M_{z,0}^2\right)}-M_{z,0}\right) \quad (151)$$

$$\frac{\partial k_{g,p}}{\partial z}(0)=\frac{-\omega/c}{1-M_{z,0}^2}\left(\sqrt{1-\left(\frac{\pi\beta_{m,n}}{R}\right)^2\left(\frac{c}{\omega}\right)^2\left(1-M_{z,0}^2\right)}+M_{z,0}\right) \quad (152)$$

$$\chi_f(0)=\frac{-i}{\omega/c-M_{z,0}\frac{\partial k_{f,p}}{\partial z}(0)} \quad (153)$$

$$\chi_g(0)=\frac{-i}{\omega/c-M_{z,0}\frac{\partial k_{g,p}}{\partial z}(0)} \quad (154)$$

$$k_{f,u}(0)=\ln\left[i\chi_f(0)\frac{\partial k_{f,p}}{\partial z}(0)\right]+k_{f,p}(0) \quad (155)$$

$$k_{g,u}(0)=\ln\left[-i\chi_g(0)\frac{\partial k_{g,p}}{\partial z}(0)\right]+k_{g,p}(0) \quad (156)$$